**PASSIVE RF TOMOGRAPHY: SIGNAL PROCESSING
AND EXPERIMENTAL VALIDATION**

THESIS

Thang M. Tran, Civilian Student

AFIT-ENG-14-M-91

**DEPARTMENT OF THE AIR FORCE
AIR UNIVERSITY**

AIR FORCE INSTITUTE OF TECHNOLOGY

Wright-Patterson Air Force Base, Ohio

AFIT-ENG-14-M-91

PASSIVE RF TOMOGRAPHY: SIGNAL PROCESSING
AND EXPERIMENTAL VALIDATION

THESIS

Presented to the Faculty

Department of Electrical Engineering

Graduate School of Engineering and Management

Air Force Institute of Technology

Air University

Air Education and Training Command

in Partial Fulfillment of the Requirements for the

Degree of Master of Science in Electrical Engineering

Thang M. Tran, B.S.E.E
Civilian Student, USAF

March 2014

PASSIVE RF TOMOGRAPHY: SIGNAL PROCESSING
AND EXPERIMENTAL VALIDATION

Thang M. Tran, B.S.E.E
Civilian Student, USAF

Approved:

//signed//	06 March 2014
Andrew J. Terzuoli, PhD (Chairman)	Date
//signed//	06 March 2014
Lorenzo Lo Monte, PhD (Member)	Date
//signed//	06 March 2014
Peter J. Collins, PhD (Member)	Date

AFIT-ENG-14-M-91

Abstract

Radio frequency (RF) tomography is an imaging technique based upon a set of distributed transmitters and receivers surrounding the area under observation. This method requires prior knowledge of the transmitters' and receivers' locations. In some circumstances the transmitters may be uncooperative, while in other cases extrinsic emitters may be used as source of opportunity. In these scenarios, RF tomography should operate in a passive modality. A previous work postulated the principles and feasibility of passive RF tomography. This research further develops the underlying theory through concise and ad-hoc signal processing. Experimental verification and validation corroborate the effectiveness of passive RF tomography for object detection and imaging.

To my grandmother, parents, and sister - I'm forever indebted to you. Your love and

sacrifices made me who I am today.

To my wife, my endless source of inspiration.

To Mr. and Mrs. Cole - I am honored to be your student and friend.

Acknowledgments

I would like to extend my gratitude towards my advisor, Dr. Terzuoli, for the opportunity to be a part of his graduate research team and his guidance to my academic achievements. I owe my future career endeavor to Dr. Terzuoli.

I would also like to give special thanks to Dr. Lo Monte, who has always been willing to spend extra time helping me with all aspects of this research from the very beginning. Dr. Lo Monte's immense knowledge, expertise, and dedication to this project were my inspiration to learn and become an RF engineer. I could not have asked for a better mentor.

I want to thank Dr. Collins for his willingness to be a member of my thesis committee. Dr. Collins has provided valuable advice and directions for my thesis and final presentation.

My sincere appreciation goes to the sponsor of this project, Mr. Scalzi from the Air Force Research Laboratory, for the chance to work on several projects at the outdoor radar range. I would also like to thank Mr. Scalzi for his time and inputs on my final presentation from the perspective of a professional engineer.

To the professors who reviewed my thesis and helped me turn it into a complete and professional document: Dr. Vaughan and Mr. Cole, thank you for your input and suggestions.

Last but definitely not least, many thanks to my lab mate and friend, Stephen Hartzell, for his help with MATLAB coding techniques.

Thang M. Tran

Table of Contents

List of Figures

Table of Symbols

Symbol	Definition
A	Attenuation
B	Bandwidth
β	Bistatic Angle
c	Speed of Light
k	Wavenumber
M	Number of Receivers
N	Number of Transmitters
P	Number of Pixels
τ	Time Delay
v	Reflectivity

Subscripts

d	Direct Path
e	Echo
m	mth Receiver
n	nth Transmitter
p	pth Object

Superscripts

a	Transmitter-related

Symbol	Definition
b	Receiver-related

List of Acronyms

Acronyms	Definition
AC	Alternating Current
ADC	Analog to Digital Converter
AFRL	Air Force Research Laboratory
AWG	Advanced Waveform Generator
CT	Computed Tomography
DAC	Digital to Analog Converter
DC	Direct Current
ELINT	Electronic Intelligence
FFT	Fast Fourier Transform
FM	Frequency Modulation
GPS	Global Positioning System
HPA	High-Power Amplifier
I	In-phase
LFM	Linear Frequency Modulation
LNA	Low-Noise Amplifier
LO	Local Oscillator
ORR	Outdoor Radar Range
PRF	Pulse Repetition Frequency
PSU	Power Supply Unit
Q	Quadrature

RF	Radio Frequency
RX	Receiver
SAR	Synthetic Aperture Radar
SNR	Signal-to-Noise Ratio
TDOA	Time Difference of Arrival
TX	Transmitter
UDRI	University of Dayton Research Institute
UPS	Uninterruptible Power Supply
WPAFB	Wright Patterson Air Force Base

PASSIVE RF TOMOGRAPHY: SIGNAL PROCESSING

AND EXPERIMENTAL VALIDATION

I. Introduction

The purpose of this research is to investigate the theory and provide experimental validation of the concept of passive RF tomography by examining the previous work on the same subject and expanding upon the obtained results. A mathematical model is developed as the backbone of the theory, followed by a hardware implementation and signal processing algorithm as a proof of concept. This research was funded by the Air Force Research Laboratory (AFRL).

1.1   Background

RF tomography is an image reconstruction method used to detect objects within an area of investigation by means of distributed transmitters and receivers. These devices are scattered around the area of interest. Their locations are known, and this information is crucial to the reconstruction methodology. Recent literature has shown increasing interest in the concept of RF tomography. Many applications such as ground penetrating radar, underground imaging, and tunnel detection have been proposed [1] [2] [3].

This research provides an extension to the groundwork of the subject by developing the theory of passive RF tomography. In its original form, RF tomography relies on the knowledge of the distributed transmitters and receivers in terms of their locations and timing. In practice, it is not always possible to deploy multiple transmitters and receivers around a region of investigation for imaging or detection purposes due to constraints in size, cost, or observability requirements of the project. Such difficulties call

for a passive approach, in which distributed receivers utilize pre-existing signals, or signals of opportunity. This unique mode of operation is named *passive RF tomography*.

Passive RF tomography is useful in many civilian as well as military applications due to the reduced size (both physical and electrical) and weight of the system. For example, emergency responders could detect and locate survivors in dangerous circumstances such as earthquakes or fires without putting lives at risk [4]. Another example is air traffic control systems for small regional airports or undeveloped countries where budgets are extremely limited. Because imaging of objects is not required, this system can rely on television and FM radio signals, which have very small bandwidth, for detection. Military applications that require covertness also could benefit from passive RF tomography because no signals are transmitted. The distributed sensors are only listening for signals of opportunity present in the area under surveillance.

1.2 Assumptions and Limitations

Passive RF tomography presents new challenges due to the lack of knowledge of transmitters and their radiated signals. In general, the locations, movements, directions, and bandwidths of the transmitters are not obvious to the receivers. Additionally, the received waveforms are not under the observer's control and may overlap, causing problems in recognizing and processing direct-path signals for matched filtering; furthermore, those incoming waves are not synchronized with the receivers, making it difficult to discern between the direct-path from transmitters and scattered signals from objects Direct path interference may also obscure the echoes from objects of interest [5]. These problems require advanced methodologies and solutions; however, some

simplifying assumptions have to be made in order to solve these problems. These assumptions are explained as follows:

Initially, the spectrum of the environment must be scanned to detect and identify signals suitable for subsequent processing. To improve resolution and simplify hardware implementation, the system should select only incoming signals with acceptable correlation properties and large duty cycles. Specifically, these waveforms are assumed to be linear frequency modulation (LFM), or chirps, and not communications waveforms. This requirement is not stringent, because virtually any terrain is illuminated with multiple radars serving various purposes such as remote sensing radars, synthetic aperture radars, early warning systems, collision avoidance systems, and weather radars [6].

Secondly, intercepted waveforms are assumed to be properly identified and separated both in time and frequency. Appropriate algorithms are used to estimate relevant parameters of each waveform such as bandwidth, chirp rate, pulse repetition frequency (PRF), duty cycle, and pulse width. Electronic intelligence (ELINT) techniques can be utilized for this task [7].

Thirdly, the incoming waveforms are assumed to be plane waves. In other words, the transmitters' locations are in the far field with respect to the receivers and objects in the scene of interest. This geometry allows the paraxial approximation to be applied to the forward signal model. This crucial theory is explained in Section 2.3 and its application to the methodology is discussed in Section 3.3.1.

Finally, it is assumed that the direct-path signal can be compressed and the echoes from objects are distinguishable. This means that in the total received signal from each

transmitter, the direct path and scattered field are not overlapped in time. This assumption is further discussed in Section 3.5.2.

1.3   Research Objectives and Scope

The research presented in this thesis focuses on two goals. First, the theory of passive RF tomography is developed and expanded based upon previous work [8]. An algorithm for the software implementation is derived from the theory. This algorithm is used to detect and localize objects within a discretized area of interest.

Finally, a proof of concept for passive RF tomography is demonstrated using experimental data based on the previously developed algorithm and methodology. As a result, a hardware prototype was built and delivered to University of Dayton Research Institute (UDRI) and AFRL. This system consists of four transmit and four receive channels, operating in the X-band with a starting frequency of 8 GHz and a bandwidth of 500 MHz. The main design goals for this test bed are: low power, light weight, mobility, and high resolution.

The scope of this research does not include Doppler processing of moving objects. Only detection and imaging of stationary objects are investigated; moreover, the hardware prototype design is not final and can be modified for future experimentation.

1.4   Methodology

The signal model presented in this thesis is built upon the foundation described in [8] with some modifications and additions to the assumptions and signal processing steps. The entire process of data acquisition, processing, and image formulation is composed of five main steps:

4

1. Identification of Signals of Opportunity – The spectrum of the surrounding environment of the observation scene is scanned, recorded, and analyzed for radar signals suitable for detection and imaging. These signals have to meet the assumptions laid out in Section 1.2. Some parts of these signals will be used as references for subsequent examination. This step is assumed to be already taken and data recorded for subsequent processing.

2. Differentiation between Incident and Scattered Signals – The focus of this research begins at this stage. Recorded signals from each receiver are separated into two distinct portions: incident and scattered fields. Incident, or direct-path signals come directly from the transmitters. Scattered signals, or echoes, are reflections from objects illuminated by the same wavefronts that made up the direct-path portion.

3. Estimation of the Time Differences of Arrivals (TDOA) – Once the signals of opportunity are identified and individualized, the TDOA for each transmitter and receiver pair and each waveform is calculated. These results are saved into a data matrix for image reconstruction.

4. Source Localization – TDOA information from the previous step is used to estimate the direction of incoming wavefronts. Because transmitters' exact locations are unknown, they have to be approximated through the bearing angles of the sources of opportunity.

5. RF Tomography in Time Domain – After the locations of the transmitters are estimated, a modified version of RF tomography is applied to the matched filtered scattered returns. The two most significant characteristics

of this step are: a) processing occurs in the time domain and b) the algorithm requires only the bearing angle information of the transmitted waveforms rather than an accurate localization of the sources.

1.5   Equipment and Facility

This research was funded by AFRL, under the supervision and leadership of AFRL/RYMD (Sensors Directorate RF Technology Branch) at Wright-Patterson Air Force Base (WPAFB). All equipment and materials for the research were provided by UDRI and AFRL. All experimentation was performed at the Outdoor Radar Range (ORR) facility at WPAFB. Data collection was accomplished by a high-performance workstation. System data sampling rate of 1.2 GS/s was achieved by an internal analog-to-digital converter (ADC) module. A full description of the test system is given in Section 4.1.

1.6   Overview

The thesis is arranged as follows: Chapter 2 explains background theories leading to the concept of passive RF tomography. Chapter 3 presents the methodologies and techniques employed in passive RF tomography. Chapter 4 demonstrates the theories in practice by applying the algorithm presented in Chapter 3 to the data acquired from the experiment. An analysis of the results is given. Chapter 5 summarizes findings, discusses successes and shortcomings as well as future work recommendations, and concludes the thesis.

Chapter 2 opens with a comparison between medical tomography using x-ray as source of radiation and radar imaging, leading to RF tomography and its passive mode of

operation. The comparison is followed by an overview of the scattering theory for bistatic radar due to the similarities between RF tomography and multistatic or bistatic radar. An important measure of performance of any bistatic radar system is the range resolution. This concept is studied along with the isorange ellipsoids and range cells. Because the transmitters are assumed to be infinitely far from the objects and receivers, the paraxial approximation is explained. Received data requires an important technique called matched filtering to increase the signal-to-noise ratio (SNR). This method of filtering is described next. Finally, this chapter concludes with an overview of recent research relevant to passive RF tomography.

Chapter 3 presents the theory expansion built upon the basic foundations described in Chapter 2 and provides a thorough understanding of passive RF tomography. The chapter defines all parameters and variables applicable to a typical layout of a real world scenario. The methodology and its five signal processing steps are discussed next. This methodology is the basis for developing the algorithm to be used in the physical experiment.

Chapter 4 describes the steps taken in the hardware experiment as well as the specifications of the system. An overview of the hardware components and schematics used in the physical experimentation is given. The chapter then compares the results of simulation and experiment conducted at the ORR facility.

The thesis is concluded with Chapter 5, which discusses the results as well as shortcomings of the results obtained in Chapter 4. Unexplored domains leading to future work are briefly recommended along with a conclusion statement.

II. Literature Review

The purpose of this chapter is to present the underlying mathematic, physics, and radar theories upon which this thesis is based. First, RF tomography is discussed in comparison to medical imaging, leading to the passive mode of operation. Because passive RF tomography is similar to multistatic radar in geometry, scattering theory for bistatic radar is explained. The Born approximation that applies to the total electromagnetic field also is explained. Consequently, a model of the scattered electric field is built upon this knowledge. In addition, the concepts of paraxial approximation and matched filtering applied in the methodology section also are discussed. Finally the range resolution relationship with the transmitted pulse is examined.

2.1 RF Tomography Background

Radar imaging and medical tomography are two inherently similar techniques [9]. They both rely on multiple perspective observations of a scene of interest to reconstruct a high resolution image of the scene. In x-ray computed tomography (CT), a three-dimensional image of an object is produced by a set of multiple two-dimensional radiographic images, or *slices*. Each of these slices is formed by measuring the attenuation information of x-rays around an axis of rotation of the object [10]. This collection of measurements provides the different views necessary to reconstruct a slice.

Similarly, in a synthetic aperture radar (SAR) system, a two-dimensional image of a terrain is obtained by illuminating the object region and observing the reflections from different perspectives, or viewing angles. This image can be created by a radar taking multiple snapshots of the area of imaging in the following manner: A radar pulse is

emitted by the radar transmitter. The backscattered electromagnetic field produced by the reflectivity of the scene is captured and recorded at the radar receiver. These radars are typically monostatic; therefore, the receiver and transmitter are at the same location. The multiple aspects are produced by varying the radar location following either a circular trajectory (spotlight SAR) or a straight line flyby (strip map SAR). Each radar snapshot of the scene is analogous to one measurement of attenuation in x-ray CT. The two key differences between x-ray CT and RF tomography are as follows: First, medical x-ray uses x-ray, which has frequencies above 30 petahertz, as source of radiation, whereas radar relies on RF sources at much lower frequencies, typically from 500 MHz up to L band at 60 GHz. Second, x-ray CT ignores phase information, which is crucial in radar image formation. Radar imaging relies on wide-band signals and small angle sub-apertures due to hardware limitations [11]. These practical constraints give rise to the concept of RF tomography in which inexpensive distributed narrowband transmitters and receivers replace the need for a monostatic radar counterpart. These scattered elements, in conjunction with their multistatic operation, provide the viewing angle diversity needed for tomographic imaging.

Passive RF tomography takes this concept one step further by eliminating the transmitters in the hardware, making the system even easier to deploy. This mode of operation relies entirely on signals of opportunity already existing in the environment; therefore, the signal processing is more challenging and requires advanced algorithms, as discussed in Section 1.2, in order to address these difficulties.

2.2 Scattering Theory for Bistatic Radar

To understand how radar pulses are reflected by objects, it is useful to build a model of the scattering wave fields. The derivation of the scattering theory in this section follows that of [12] with some modifications to fit the notations and parameter definitions in this thesis.

Throughout this thesis, the notation of parameters follows standard rules. Bold letters denote three-dimensional vectors. The carets ($\wedge$) on vectors signify that they are unit vectors. Bold and capital letters designate matrices.

Consider a bistatic scenario in which an isotropic source located at $\mathbf{r}_n^a$ radiates a vector electromagnetic field in all directions into free space. This electromagnetic field is defined as the incident field, denoted by $\mathbf{E}^{in}$, with respect to the object. The region of interest of which an image is to be constructed is discretized into P pixels. If there is an object located at $\mathbf{r}_p$, the field scatters in a manner similar to how it was transmitted from the source. The scattered field, $\mathbf{E}^{sc}$, is recorded by a receiver at $\mathbf{r}_m^b$. Assume that the objects do not have any depolarization effects on the incident field; therefore, $\mathbf{E}^{in}$ and $\mathbf{E}^{sc}$ have the same polarization. Moreover, individual objects are assumed to be isotropic. These two common assumptions make it possible to simplify the vector wave equation into a scalar equation without changing its meaning.

The scalar scattered field E^{sc} and incident field E^{in} together satisfy the decomposition of the total field E^{tot} as follows:

$$E^{tot} = E^{in} + E^{sc} \tag{2.1}$$

In terms of the transmitter-object distance, the incident field can be defined as

$$E^{in} = \frac{e^{jk\|\mathbf{r}_n^a - \mathbf{r}_p\|}}{4\pi \|\mathbf{r}_n^a - \mathbf{r}_p\|} \qquad (2.2)$$

where $k = \dfrac{2\pi}{\lambda}$ is the wavenumber with λ being the wavelength of the incoming wave.

In radar signal processing, the scattered field is measured at the receiver. Mathematically, the scattered field can be modeled in the frequency domain as

$$E^{sc}(\omega, \mathbf{r}_n^a, \mathbf{r}_m^b) = \iiint \frac{e^{jk\|\mathbf{r}_p - \mathbf{r}_m^b\|}}{4\pi \|\mathbf{r}_p - \mathbf{r}_m^b\|} v(\mathbf{r}_p) E^{tot}(\omega, \mathbf{r}_p) d\mathbf{r}_p \qquad (2.3)$$

where $v(\mathbf{r}_p)$ is the reflectivity corresponding to the pth pixel of the discretized scene of interest [12].

The scattered field cannot be solved from Equation (2.3) because E^{sc} is included in E^{tot}, as explained in Equation (2.1). Furthermore, $v(\mathbf{r}_p)$ is the unknown of the imaging problem, and is multiplied by the another unknown, E^{sc}, contained within E^{tot}. The Born approximation can be applied to the total electric field on the right hand side of Equation (2.3), replacing it with the known incident field, E^{in} [12]. This approximation makes it linear and allows the scattered field to be solvable by

$$E^{sc}(\omega, \mathbf{r}_n^a, \mathbf{r}_m^b) = \iiint \frac{e^{jk\|\mathbf{r}_p - \mathbf{r}_m^b\|}}{4\pi \|\mathbf{r}_p - \mathbf{r}_m^b\|} v(\mathbf{r}_p) E^{in}(\omega, \mathbf{r}_p) d\mathbf{r}_p \qquad (2.4)$$

Substituting Equation (2.2) into (2.4) gives the following:

$$E^{sc}(\omega, \mathbf{r}_n^a, \mathbf{r}_m^b) = \iiint \frac{e^{jk\left(\|\mathbf{r}_n^a - \mathbf{r}_p\| + \|\mathbf{r}_p - \mathbf{r}_m^b\|\right)}}{16\pi^2 \|\mathbf{r}_n^a - \mathbf{r}_p\| \|\mathbf{r}_p - \mathbf{r}_m^b\|} v(\mathbf{r}_p) d\mathbf{r}_p \qquad (2.5)$$

11

Next, the Fourier transform is applied to Equation (2.5), converting this expression to the time domain. The incident field E^{in} becomes the time signal from a transmitter, $s_n[t]$, delayed by the time it takes for the signal to travel from the transmitter to the object, then from the object to the receiver. The process is explained as follows:

$$
\begin{aligned}
E^{sc}(t,\mathbf{r}_n^a,\mathbf{r}_m^b) &= \int E^{sc}(\omega,\mathbf{r}_n^a,\mathbf{r}_m^b)e^{j\omega t}\, d\omega \\
&= \int \iiint \frac{e^{jk\left(\left\|\mathbf{r}_n^a-\mathbf{r}_p\right\|+\left\|\mathbf{r}_p-\mathbf{r}_m^b\right\|\right)}}{16\pi^2\left\|\mathbf{r}_n^a-\mathbf{r}_p\right\|\left\|\mathbf{r}_p-\mathbf{r}_m^b\right\|}v(\mathbf{r}_p)d\mathbf{r}_p\, e^{j\omega t}\, d\omega \\
&= \iiint s_n\left[t-\left\|\mathbf{r}_n^a-\mathbf{r}_p\right\|/c-\left\|\mathbf{r}_p-\mathbf{r}_m^b\right\|/c\right]\frac{v(\mathbf{r}_p)}{16\pi^2\left\|\mathbf{r}_n^a-\mathbf{r}_p\right\|\left\|\mathbf{r}_p-\mathbf{r}_m^b\right\|}d\mathbf{r}_p
\end{aligned}
\tag{2.6}
$$

For a discretized scene of interest, where the area of investigation is divided into P pixels, this scattered field is rewritten as follows:

$$
E^{sc}(\mathrm{t},\mathbf{r}_n^a,\mathbf{r}_m^b) = \sum_{p=1}^{P}\left\{ s_n\left[t-\left\|\mathbf{r}_n^a-\mathbf{r}_p\right\|/c-\left\|\mathbf{r}_p-\mathbf{r}_m^b\right\|/c\right]\frac{v(\mathbf{r}_p)}{16\pi^2\left\|\mathbf{r}_n^a-\mathbf{r}_p\right\|\left\|\mathbf{r}_p-\mathbf{r}_m^b\right\|}\right\}
\tag{2.7}
$$

Equation (2.7) is equivalent to the model of the scattered signal recorded by the receiver located at $\mathbf{r}_m^b$ due to incoming waves from the transmitter at $\mathbf{r}_n^a$. This signal is the superposition of echoes from all P pixels within the scene of investigation; therefore, it is summed to P. Equation (2.7) is the foundation of the forward model of passive RF tomography and is further studied in Chapter 3.

2.3   Paraxial Approximation

In Gaussian optics, the paraxial approximation is applied when a ray of light makes a small angle to the path of propagation [13]. This happens when the paraxial ray

lies close to the optical axis or when the source is considered infinitely far from the optical system.

In radar terms, a ray is any line from an isolated source generated in any direction. In other words, a ray defines the direction of wave propagation, and it is normal to the surface of constant phase of a wavefront [14]. For most radars, objects are in the far field with respect to the transmitter and are physically small enough for the illuminating spherical waves to be approximated as planewaves. This approximation yields an important result: Because the wavefronts are planar, their defining rays from the source are parallel and are perpendicular to the wavefronts. Figure 1 illustrates the paraxial approximation where the source-object range R is much larger than the object size L. The spherical wavefront (solid) is approximated by the planewave front (dashed). The two defining rays, 1 and 2, are parallel to each other.
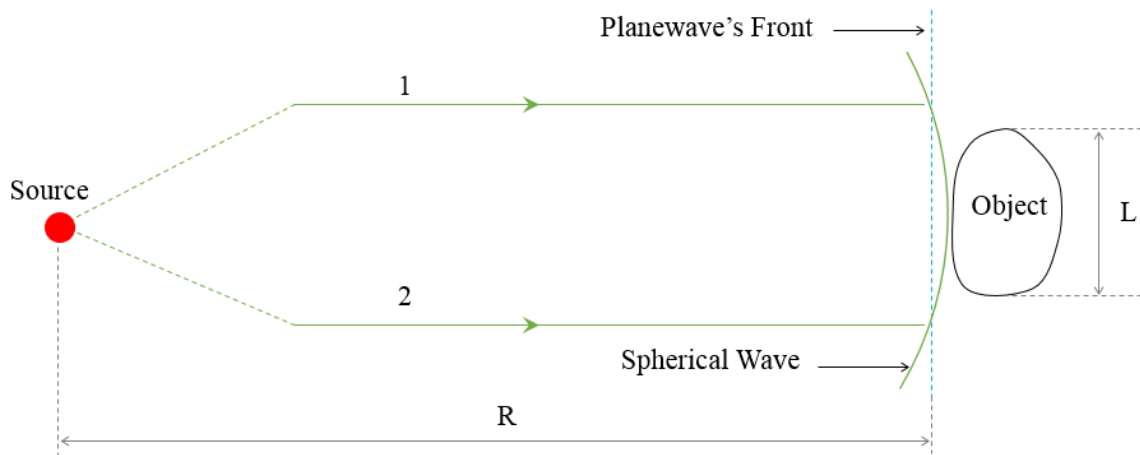
Figure 1: Paraxial approximation of a spherical wavefront when the source is sufficiently far from the object

2.4   Matched Filtering

In radar signal processing, matched filtering refers to an important technique to maximize the SNR in received signals. Usually, useful information such as echoes from radar objects is buried within noise and other interference. Detection of these objects requires a comparison of the total received waveforms with the known transmitted signal. Thus, a filter has to be designed for such a task [15].

The matched filter in its original form is a linear filter. It is obtained by correlating a received unknown signal with a template to produce an output sequence which maximizes at locations where the template is detected in the received signal [16]. The brief derivation of this type of filter is based on [17], as follows: Suppose $x(t)$ is the unknown received signal which contains a useful and known radar signal $s(t)$ in addition to white noise $n(t)$, i.e.,

$$y(t) = s(t) + n(t) \tag{2.8}$$

A filter with impulse response $h(t)$ is to be designed in order to maximize the SNR in $y(t)$. By definition of matched filters, the impulse response of such filter is the replica of the transmitted waveform that has been reversed in time and conjugated [17], i.e.,

$$h(t) = s(T - t) \tag{2.9}$$

where T is the length of the reference signal $s(t)$.

The output of the matched filter, $y_f(\tau)$, is defined as follows:

$$y_f(\tau) = \int y(\tau)h(\tau)d\tau = \int y(\tau)s(T-\tau)d\tau \tag{2.10}$$

To visualize this filter and its output when applied to the received signal, consider the following example. Let $s(t)$ be an LFM chirp of length of 1 second. The received signal is 8 seconds long and contains both the chirp and a white noise with power four times greater than the signal power, i.e., the SNR of the total received signal is −6 dB. The chirp starts at $t = 4$ seconds in the received signal as illustrated in Figure 2 (a) and (b). In the matched-filtered signal, a strong peak appears at $\tau = 4$, corresponding to the location of $s(t)$ inside $y(t)$.
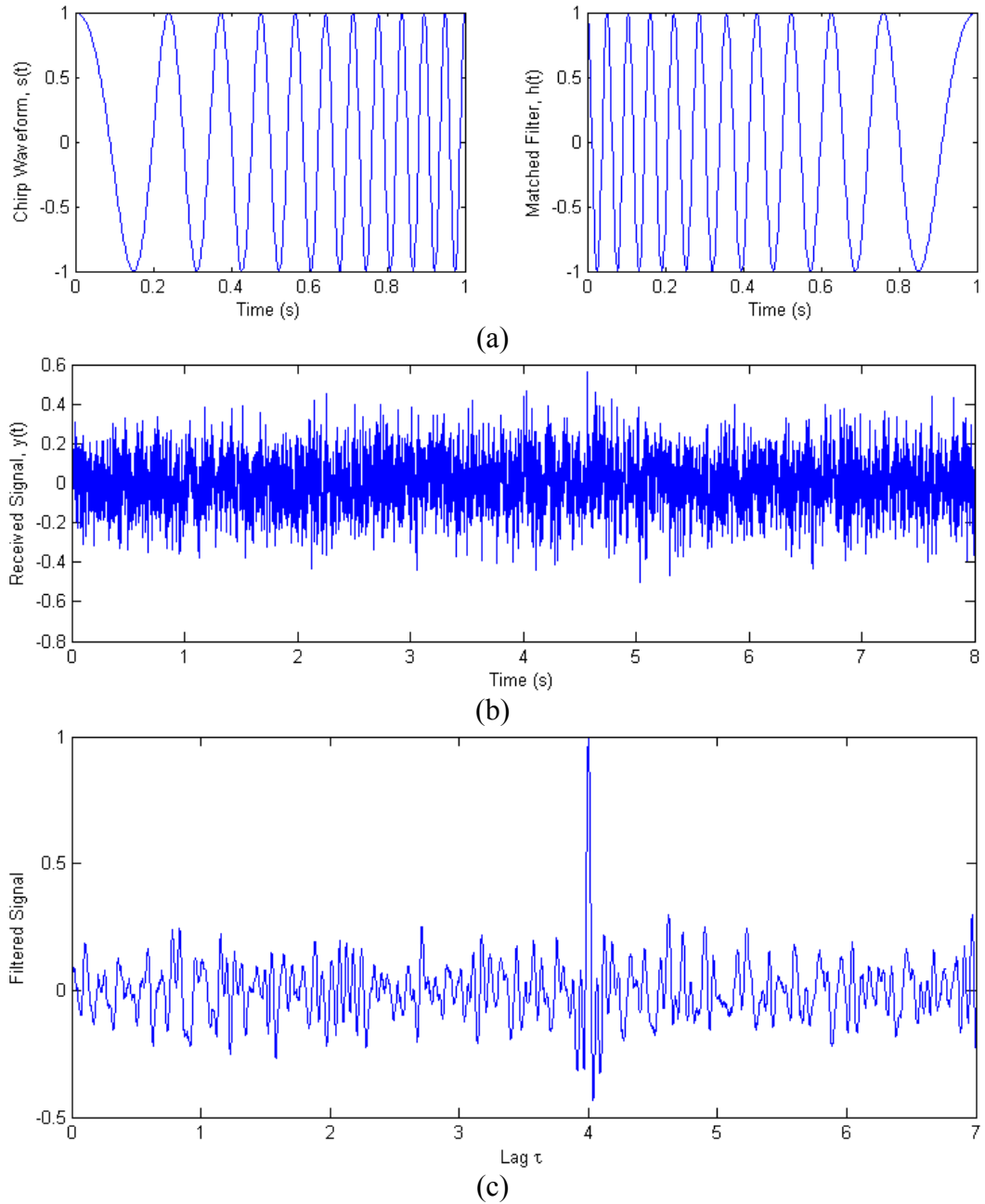
Figure 2: Matched filtering: (a) Original chirp *s(t)* and the impulse response of the match filter *h(t)*; (b) Total received signal with SNR = −6 dB; (c) Matched filtered signal with peak at $\tau = 4$ seconds

2.5   Bistatic Range Resolution

An important characteristic as well as performance measurement of any radar system is the range resolution. This quantity can be derived from the isorange ellipsoids and range cells. The following is applicable to both bistatic and passive RF tomography.

2.5.1   Isorange Ellipsoids

Consider a simple bistatic radar case with one transmitter, one receiver, and one object. The plane in which they all lie is called the *bistatic plane*. Let L, R_T, R_R denote the ranges between transmitter-receiver, transmitter-object, and receiver-object, respectively; β is the bistatic angle, measured between the transmitter and receiver from the perspective of the object.

The transmitter-object-receiver range is measured by the sum $R_T + R_R = 2a$, where *2a* is the major axis of the ellipsoid.. This sum represents the set of all possible locations of the object with respect to the transmitter and receiver. When plotted, it is the surface of an ellipsoid whose foci coincide with the transmitter's and receiver's locations. This ellipsoid is completely defined by the baseline L and major axis $2a$. It is conventionally regarded as the isorange ellipsoid of constant range sum $2a$. Figure 3 illustrates an intersection of the isorange ellipsoid with a bistatic plane which contains the transmitter, receiver, and object. This intersection is commonly referred to as the isorange contour. In the monostatic case, the analogous isorange ellipsoid is a sphere with radius a (when $L = 0$). Consequently, the monostatic isorange contour is a circle whose center coincides with the transmitter and receiver. In addition, the object's SNR and range resolution vary as a function of its position on a constant range sum contour. This

variation is caused by the dependence of SNR and range resolution of the object on the

bistatic angle β, which varies according to the object's position [18]. This causes

significant differences in the operation of bistatic radars compared to monostatic radars.
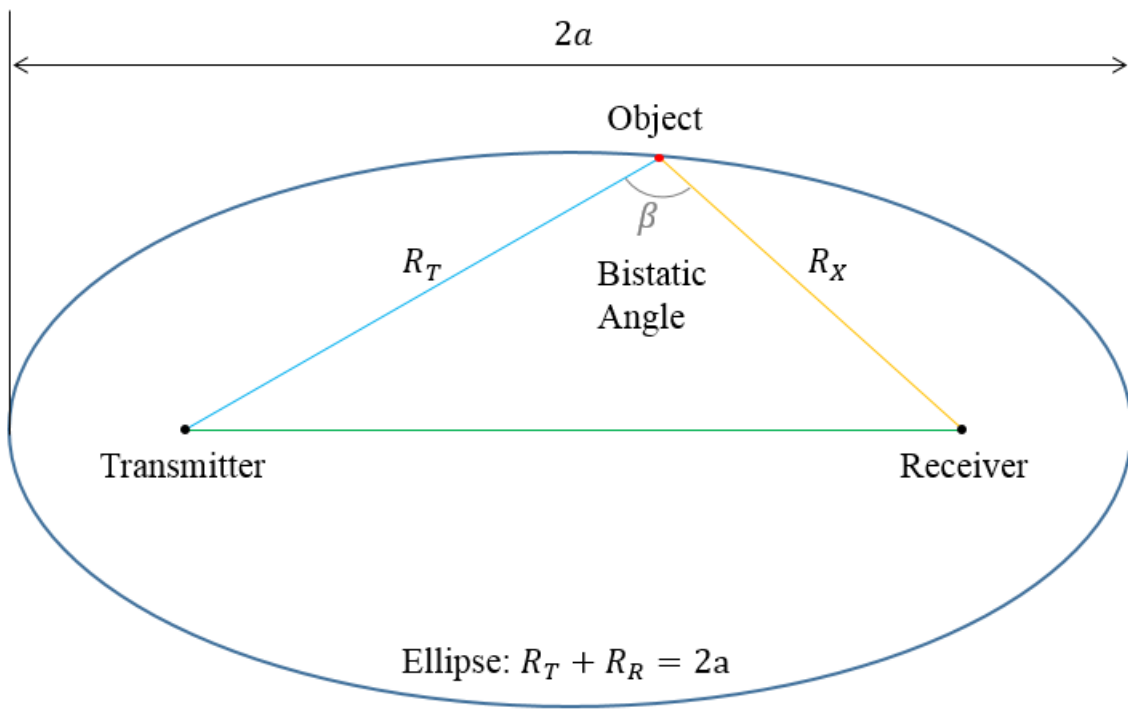
Figure 3: Ellipse of constant range sum, or isorange contour.

2.5.2 Range Cells

For the monostatic case, a range cell is defined as the minimum separation in distance

between two isotropic objects that is discernible at the receiver [18]. In terms of the

radar's compressed pulsewidth, τ, this quantity is defined as

$$r_M = \frac{c\tau}{2} = \frac{c}{2B} \tag{2.11}$$

where c is the speed of light and B is the bandwidth of the transmitted pulse.

18

In other words, a monostatic range cell is the distance between two concentric

isorange contour circles. Similarly, a bistatic range cell, r_B, is defined to be the gap

between two confocal isorange contour ellipses, i.e., $R'_T + R'_R = 2a'$ and $R_T + R_R = 2a$

where $a' > a$ and $a' - a = r_B$ This length, unlike its monostatic counterpart, is not

constant. Instead, it varies and is measured along the bisector of the bistatic angle β of

the inner ellipse. The geometry for this bistatic range cell is illustrated in Figure 4.
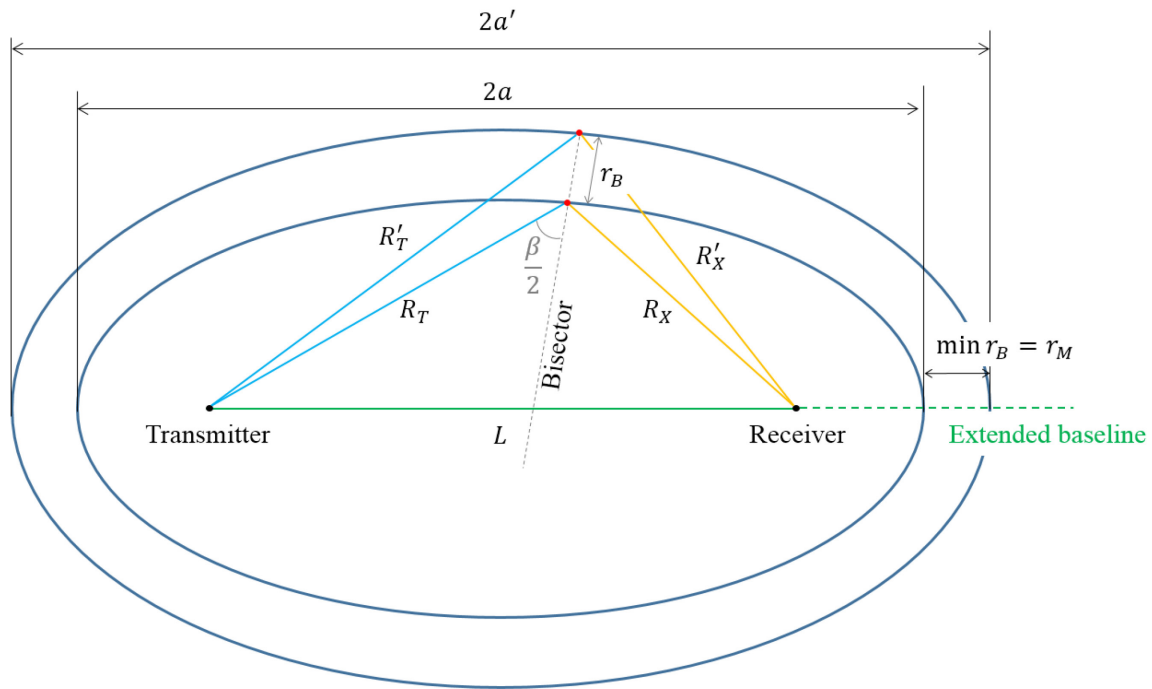
Figure 4: Bistatic range cell (r_B)

When the object location changes on the isorange contour, the bistatic range cell

reaches maximum when β is also at its maximum, which is when $R_T = R_R$ and the

bisector of the bistatic angle is perpendicular to the baseline. Similarly, when β is

minimum, i.e., 0°, the bistatic range cell is at its minimum, as illustrated in Figure 4. This value is the pseudomonostatic range cell and is defined as

$$r_M = a' - a = \frac{c\tau}{2} \tag{2.12}$$

The bistatic range cell r_B can be approximated in terms of β and τ with negligible error as follows [18]:

$$
\begin{aligned}
r_B &= \frac{r_M}{\cos(\beta/2)} \\
&= \frac{c\tau}{2\cos(\beta/2)}
\end{aligned}
\tag{2.13}
$$

This important result is used to calculate the range resolution for any bistatic radar.

2.5.3   Range Resolution

For any two objects to be distinguishable at the bistatic receiver, their spatial separation has to be at least $c\tau/2$ [19]. This condition is satisfied if the two objects lie on two adjacent bistatic isorange contours with a separation of approximately

$r_B = \dfrac{c\tau}{2\cos(\beta/2)}$, as described in Equation (2.13). Clearly, as long as the two objects are

at least r_B apart from each other, they are distinguishable at the receiver.

This estimation is no longer valid when $\dfrac{\beta}{2} = 90°$ or $\beta = 180°$, which is when the transmitter, object, and receiver are positioned on a straight line in that order. This special case can be ignored because when β approaches 180°, the object is in the blind region of

the receiver, and its echoes are indistinguishable from the direct-path signal. This area is further studied in Section 3.5.2.

2.6   Relevant Research

Recent developments have shown preliminary results in RF tomography applications. Using distributed sensors and transmitters, researchers at AFRL and UDRI were able to simulate the detection of anomalies embedded in an underground region [20] [21]. Experimental results also were achieved in the applications of underground radar and tunnel detection [22] [23]. These methodologies and results are the basis and motivation for this research.

In parallel, researchers at the Warsaw University of Technology published a series of papers on passive radar theories and experiments. They used various analog as well as digital signals as sources of opportunities. These include FM radio, digital television, cellular phones, and wireless signals (WiFi and WiMax) [24]. After multiple trials, they were able to produce results for tracking military objects during a 2011 exercise in Poland [25]. In a related research, they used the same hardware setup and were capable of detecting commercial airplanes at long ranges (around 285 km) by utilizing high-powered FM transmitters [26]. In a different passive SAR imaging experiment using a satellite pulsed radar as the source of opportunity, researchers successfully produced an image of several man-made objects [27]. This result shows that it is possible to form a SAR image using a stationary receiver and a non-cooperative source mounted on a moving platform.

2.7   Summary

The background theories presented in this chapter are the basis of the methodology and resulting algorithm for image reconstruction. In the next chapter, the signal processing steps are derived. The methodology is developed for a typical scenario of a pixelated, or discretized, scene of interest in which objects may be present. This region is surrounded by scattered receivers which provide the different perspective views necessary to form a passive RF tomography image.

III. Methodology

This chapter explains the technique as well as a detailed procedure in the processing of experimental data. All variables and parameters are defined for a typical layout of a real world scenario. Then, the signal processing is explained step by step in detail. This methodology provides the blueprint for a hardware experiment setup and image reconstruction algorithm discussed in Chapter IV.

3.1   Definition of Parameters

Consider a scenario in which a region of interest is illuminated by N transmitters and surrounded by M receivers. Each transmitter is located at position

$\mathbf{r}_n^a = x_n^a \hat{\mathbf{x}} + y_n^a \hat{\mathbf{y}} + z_n^a \hat{\mathbf{z}}$ and each receiver at $\mathbf{r}_m^b = x_m^b \hat{\mathbf{x}} + y_m^b \hat{\mathbf{y}} + z_m^b \hat{\mathbf{z}}$. Every transmitter

radiates a unique waveform $s_n[t]$. As stated in Chapter 1, it is assumed that all sensors share a common reference signal for timing, such as the global positioning system (GPS), and that their positions are known with negligible errors.

The region of interest is discretized into P pixels, where each one is centered at the vector $\mathbf{r}_p = x_p \hat{\mathbf{x}} + y_p \hat{\mathbf{y}} + z_p \hat{\mathbf{z}}$ where $p = 1, 2, \ldots, P$. If an object is present at the pth pixel, an isotropic scattered wave is generated with reflectivity v_p. Conversely, if no object is present at pixel p, $v_p = 0$. The imaging problem is equivalent to an estimation of all v_p, given measured data from distributed sensors.

3.2   Differentiation between Direct-Path and Scattered Signals

First, a model has to be established for the signal received at the mth receiver. This signal consists of two components: a direct-path and scatter from objects. The first

23

component comes directly from each transmitter, hence the name direct-path signal. It is the original signal $s_n[t]$ generated by the nth transmitter and delayed by $\left\| \mathbf{r}_n^a - \mathbf{r}_m^b \right\|/c$ seconds, which is the time it takes for the transmitted signal to reach the mth receiver. Additionally, due to an unknown T_n seconds delay in transmission of each transmitter, the total direct-path signal recorded at the mth receiver due to the wavefront from the nth transmitter becomes

$$E_{nm}^d[t] = A_{nm} s_n\left[t - \left\| \mathbf{r}_n^a - \mathbf{r}_m^b \right\|/c - T_n \right] \tag{3.1}$$

where $A_{mn} = \dfrac{1}{4\pi \left\| \mathbf{r}_n^a - \mathbf{r}_m^b \right\|}$ is the amplitude of signal received at the mth receiver due to the wavefront from the nth transmitter.

Each transmitted signal also produces scattered signals, or echoes, from different isotropic objects in the investigation region. These signals compose the second component of the total received signal at the mth receiver. Similar to the behavior of the direct-path signal, the echoes are also a delayed version of $s_n[t]$. This temporal delay is equal the time it takes for the original signal to travel from the nth transmitter to the pth object, then from the pth object to the mth receiver. This delay in terms of positional vectors is $\left\| \mathbf{r}_n^a - \mathbf{r}_p \right\|/c + \left\| \mathbf{r}_p - \mathbf{r}_m^b \right\|/c$. Because there are P objects, these echoes are summed to P to form the total echoes received at the mth receiver as follows:

$$E_{nm}^e[t] = \sum_{p=1}^{P}\left\{ A_{pm} v_p s_n\left[t - \left\| \mathbf{r}_n^a - \mathbf{r}_p \right\|/c - \left\| \mathbf{r}_p - \mathbf{r}_m^b \right\|/c - T_n \right] \right\} \tag{3.2}$$

where $A_{pm} v_p$ is the amplitude of the echo from an isotropic object present at the pth pixel captured at the mth receiver due to the wavefront from the nth transmitter.

24

Finally, because there are N transmitters, the total received signal at any receiver is a sum of all direct-path signals from N transmitters and the associated echoes produced by them. Thus, the total received signal at the mth receiver due to N transmitters and P objects is

$$
\begin{aligned}
E_m[t] &= \sum_{n=1}^{N} \left\{ \rho_{nm}^{d}[t] + \rho_{nm}^{e}[t] \right\} \\
&= \sum_{n=1}^{N} \left\{ A_{nm} s_n \left[t - \left\| \mathbf{r}_n^a - \mathbf{r}_m^b \right\| / c - T_n \right] \right. \\
&\quad \left. + \sum_{p=1}^{P} \left[A_{pm} v_p s_n \left[t - \left\| \mathbf{r}_n^a - \mathbf{r}_p \right\| / c - \left\| \mathbf{r}_p - \mathbf{r}_m^b \right\| / c - T_n \right] \right] \right\}
\end{aligned}
\tag{3.3}
$$

where $c =$ speed of light.

$m = 0, 1, ..., M$ - number of receivers

$n = 0, 1, ..., N$ - number of transmitters

$T_n =$ time delay of each transmitter due to different time of transmission

Note that A_{nm} is much greater than $A_{pm} v_p$ because only a small portion of the transmitted signal is scattered by the object; furthermore, the scattered signal is presumed to be isolated in time. Figure 5 illustrates the geometry and range delays in the received signal model at one receiver due to illuminating waves from one transmitter.
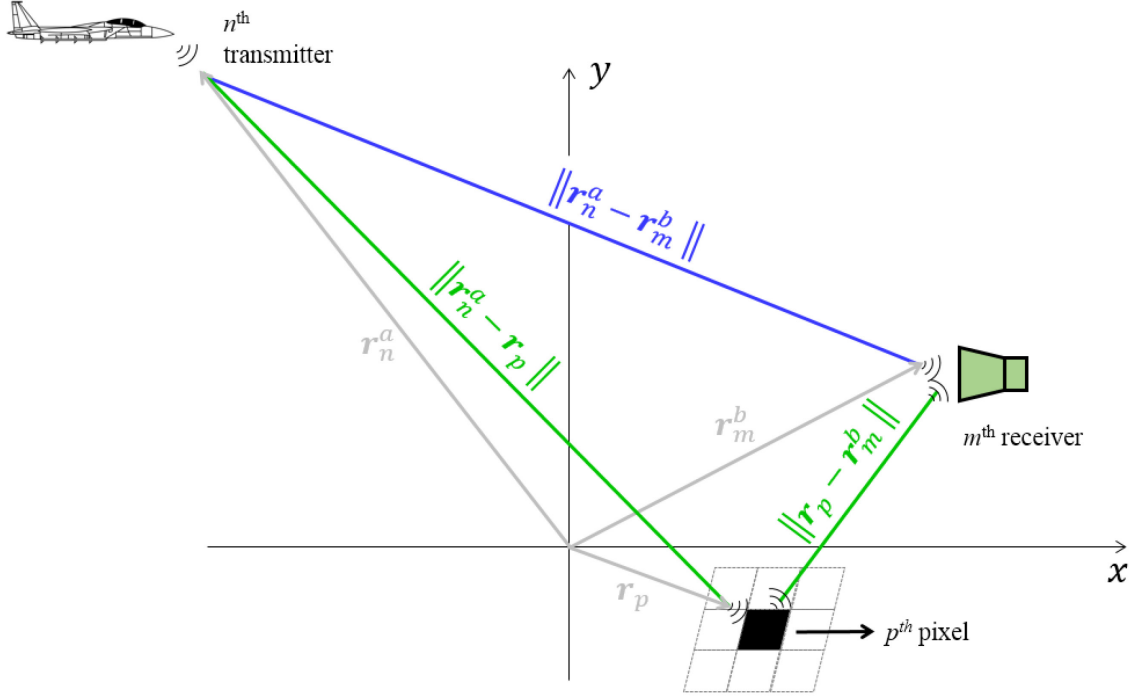
Figure 5: Explanation of the received signal model at the mth receiver due to waves from the nth transmitter

An accurate tomographic reconstruction requires the exact locations of both transmitters and receivers. Because the transmitters are assumed to be much farther away than the distributed receivers, it is difficult to estimate their positions in the presence of noise. To make the problem solvable, only the directions of the transmitters need to be estimated; as a result, the transmitter locations in the forward model for RF tomography are eliminated and substituted with only the information of the directions of their radiated waveforms. To achieve this, Equation (3.3) is expressed in terms of the receivers' positions, the pixels under observation, and the directions of propagation of the transmitted waves. Two steps are required for this estimation: 1) Apply the paraxial approximation and 2) Substitute the result in Equation (3.3).

3.3   Estimation of the Time Difference of Arrival

To eliminate all unknown quantities later in the matched filtered signal, the transmitter-object distance from Equation (3.3), $\left\| \mathbf{r}_n^a - \mathbf{r}_p \right\|$, is replaced by an estimation based on the transmitter-receiver separation, $\left\| \mathbf{r}_n^a - \mathbf{r}_m^b \right\|$, and the direction of incoming waves from the transmitter. This estimation is based on the paraxial approximation due to the assumption that transmitters are infinitely far from the receivers and objects.

3.3.1   Paraxial Approximation

Consider the scene of interest as shown in Figure 6. Let unit vector $\hat{\mathbf{n}}_n^a$ denote the normal direction of the wave generated by the nth transmitter. In other words, $\hat{\mathbf{n}}_n^a$ is the direction of the incoming waveforms.
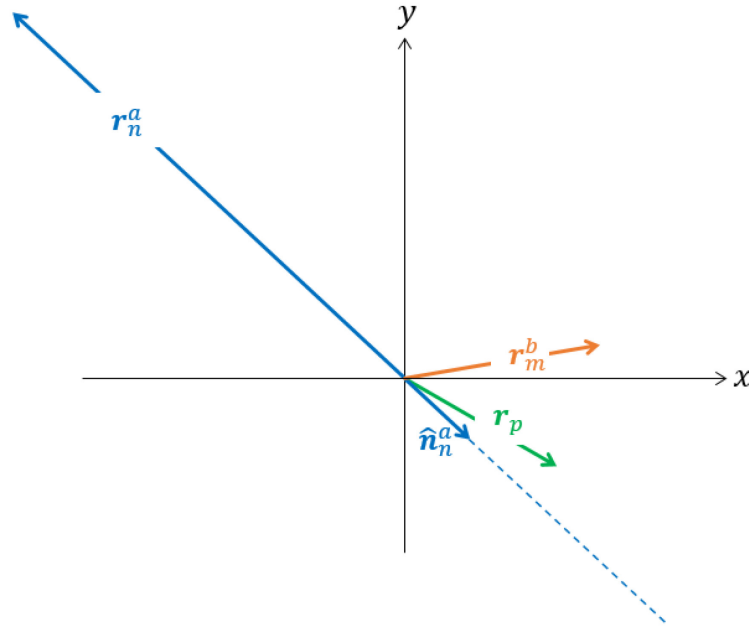
Figure 6: Geometry of the scene of interest

Because the transmitters are assumed to be much farther away than the transmitters and objects, vectors $\mathbf{r}_n^a$, $\mathbf{r}_n^a - \mathbf{r}_m^b$, and $\mathbf{r}_n^a - \mathbf{r}_p$ are approximately parallel, as shown in Figure 7.
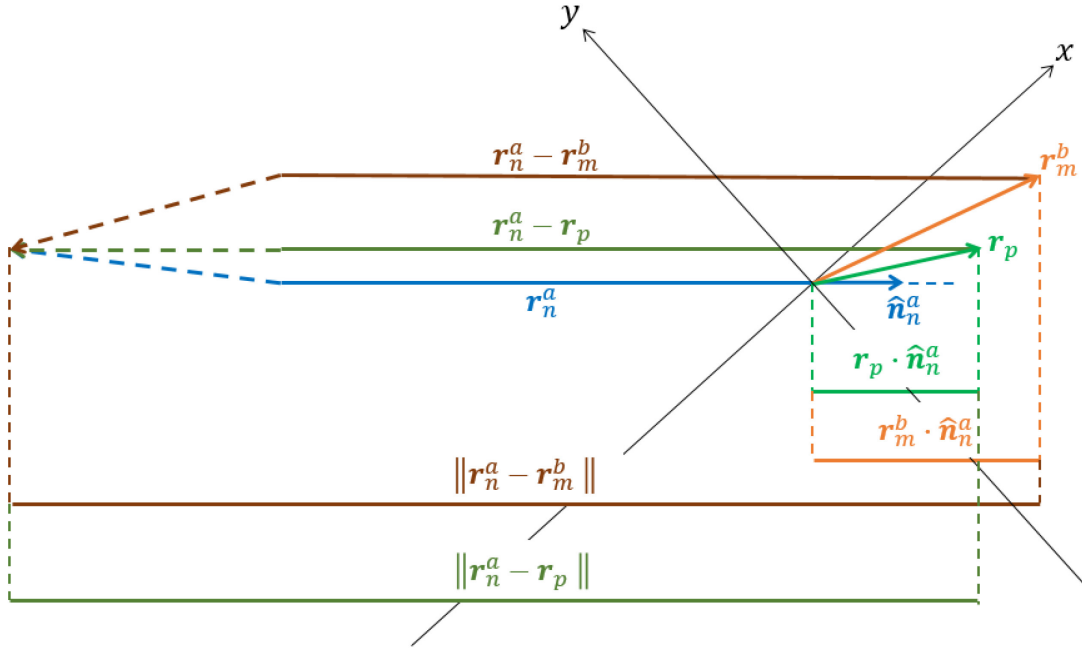
Figure 7: Paraxial approximation

From this parallel approximation, it is easy to see that

$$\left\| \mathbf{r}_n^a - \mathbf{r}_p \right\| = \left\| \mathbf{r}_n^a - \mathbf{r}_m^b \right\| - \mathbf{r}_m^b \cdot \hat{\mathbf{n}}_n^a + \mathbf{r}_p \cdot \hat{\mathbf{n}}_n^a \tag{3.4}$$

or

$$\left\| \mathbf{r}_n^a - \mathbf{r}_p \right\| = \left\| \mathbf{r}_n^a - \mathbf{r}_m^b \right\| + \left(\mathbf{r}_p - \mathbf{r}_m^b \right) \cdot \hat{\mathbf{n}}_n^a \tag{3.5}$$

This result is only true if and only if $\left\|\mathbf{r}_n^a\right\| \gg \left\|\mathbf{r}_m^b\right\|$. The approximation obtained

from Equation (3.5) is then substituted back into Equation (3.3) to yield the following:

$$
\begin{aligned}
E_m[t] = \sum_{n=1}^{N} \Big\{ & A_{nm} s_n \left[t - \left\|\mathbf{r}_n^a - \mathbf{r}_m^b\right\| / c - T_n \right] \\
& + \sum_{p=1}^{P} A_{pm} v_p s_n \left[t - \left(\left\|\mathbf{r}_n^a - \mathbf{r}_m^b\right\| + \left[\mathbf{r}_p - \mathbf{r}_m^b \right] \cdot \hat{\mathbf{n}}_n^a \right) / c - \left\|\mathbf{r}_p - \mathbf{r}_m^b\right\| / c - T_n \right] \Big\}
\end{aligned}
$$

(3.6)

Although this equation appears to be more complicated than Equation (3.3), it is

actually more suitable for the purpose of eliminating the unknown quantity, i.e., the

location of the *n*-transmitter after matched filtering with the direct-path signal.

3.3.2 Matched Filtering of the Received Signal

To localize the sources, the TDOA of the transmitters have to be determined by

means of matched filtering. Because no transmitters' signals are used as reference for

matched filtering, the direct-path signal has to be isolated and used for that purpose.

Recall from Chapter 1 that all transmitted signals are assumed to be separable in time and

frequency. This assumption means the transmitters' signals do not overlap with each

other and makes it possible to distinguish the signal from each transmitter at the receivers

by means of filtering; consequently, the signal recorded at each receiver can be divided

into multiple portions, each coming from a different transmitter, i.e.,

$$
\begin{aligned}
E_{nm}[t] = A_{nm} s_n & \left[t - \left\|\mathbf{r}_n^a - \mathbf{r}_m^b\right\| / c - T_n \right] \\
& \sum_{p=1}^{P} A_{pm} v_p s_n \left[t - \left(\left\|\mathbf{r}_n^a - \mathbf{r}_m^b\right\| + \left[\mathbf{r}_p - \mathbf{r}_m^b \right] \cdot \hat{\mathbf{n}}_n^a \right) / c - \left\|\mathbf{r}_p - \mathbf{r}_m^b\right\| / c - T_n \right] \Big\}
\end{aligned}
$$

(3.7)

Evidently, this expression does not contain the sum from $n = 1$ to N when

compared to that of Equation (3.6). To simplify notation, let

$$
X = \left\|\mathbf{r}_n^a - \mathbf{r}_m^b\right\| / c + T_n
$$

29

and

$$Y = \frac{\left\| \mathbf{r}_p - \mathbf{r}_m^b \right\| + \left[\mathbf{r}_p - \mathbf{r}_m^b \right] \cdot \hat{\mathbf{n}}_n^a}{c}$$

Equation (3.7) becomes:

$$E_{nm}[t] = A_{nm} s_n [t - X] + \sum_{p=1}^{P} A_{pm} v_p s_n [t - X - Y] \qquad (3.8)$$

Because the direct-path signal is assumed to be separated from the backscatters, $s_n [t - X]$ is separable from $E_{nm}[t]$ by means of gating. The total signal, $E_{nm}[t]$, is then matched filtered with $s_n [t - X]$ from the nth transmitter to produce a column vector $\mathbf{t}_{nm}$.

This process can be broken down into two smaller steps due to linearity. Let $\star$ denote the cross-correlation operation. By cross-correlation definition, the following is true:

$$\mathbf{t}_{nm}[\tau] = s_n [t - X] \star E_{nm}[t]$$
$$= \underbrace{\left\{ s_n[t - X] \star A_{nm} s_n [t - X] \right\}}_{C_1} + \underbrace{\left\{ s_n[t - X] \star \sum_{p=1}^{P} A_{pm} v_p s_n [t - X - Y] \right\}}_{C_2} \qquad (3.9)$$

Consider C_1

$$\begin{aligned} C_1 &= A_{nm} \left\{ s_n[t - X] \star s_n [t - X] \right\} \\ &= A_{nm} r_s[\tau] \end{aligned} \qquad (3.10)$$

where $r_s[\tau]$ is the auto correlation sequence of $s_n[t]$ and the domain of $r_s[\tau]$ is from $-T_s$ to T_s.

By linearity, C_2 becomes the following:

$$C_2 = \sum_{p=1}^{P} A_{pm} v_p \left\{ s_n[t-X] \star s_n[t-X-Y] \right\}$$
$$= \sum_{p=1}^{P} A_{pm} v_p r_s[\tau - Y]$$

(3.11)

and therefore,

$$\mathbf{t}_{nm}[\tau] = A_{nm} r_s[\tau - X] + \sum_{p=1}^{P} A_{pm} v_p r_s[\tau - Y]$$
$$= A_{mn} r_s[\tau] + \sum_{p=1}^{P} A_{pm} v_p r_s \left[\tau - \frac{\left\| \mathbf{r}_p - \mathbf{r}_m^b \right\|}{c} - \frac{\left(\mathbf{r}_p - \mathbf{r}_m^b \right) \cdot \hat{\mathbf{n}}_n^a}{c} \right]$$

(3.12)

Equation (3.12) is the received signal after matched filtering. This important outcome will be used for the forward model of the time domain RF tomography.

Equation (3.12) is subsequently used to determine v_p; however, it still contains an unknown quantity: $\hat{\mathbf{n}}_n^a$. This vector can be estimated in a process called source localization which, as the name implies, approximates the transmitter's location based on the assumption that it is infinitely far from the scene of imaging. The process is explained in the next section.

3.4   Source Localization

Let d_{ij} denote the range difference between sensors, as seen by the approaching transmitted waves. From Figure 8, this distance is equal to the difference between $\mathbf{r}_n^a - \mathbf{r}_i^b$ and $\mathbf{r}_n^a - \mathbf{r}_j^b$ projected onto the wavefront traveling direction $\hat{\mathbf{n}}_n^a$, i.e.,

$$d_{ij} = \left\| \mathbf{r}_n^a - \mathbf{r}_i^b \right\| - \left\| \mathbf{r}_n^a - \mathbf{r}_j^b \right\|$$

(3.13)
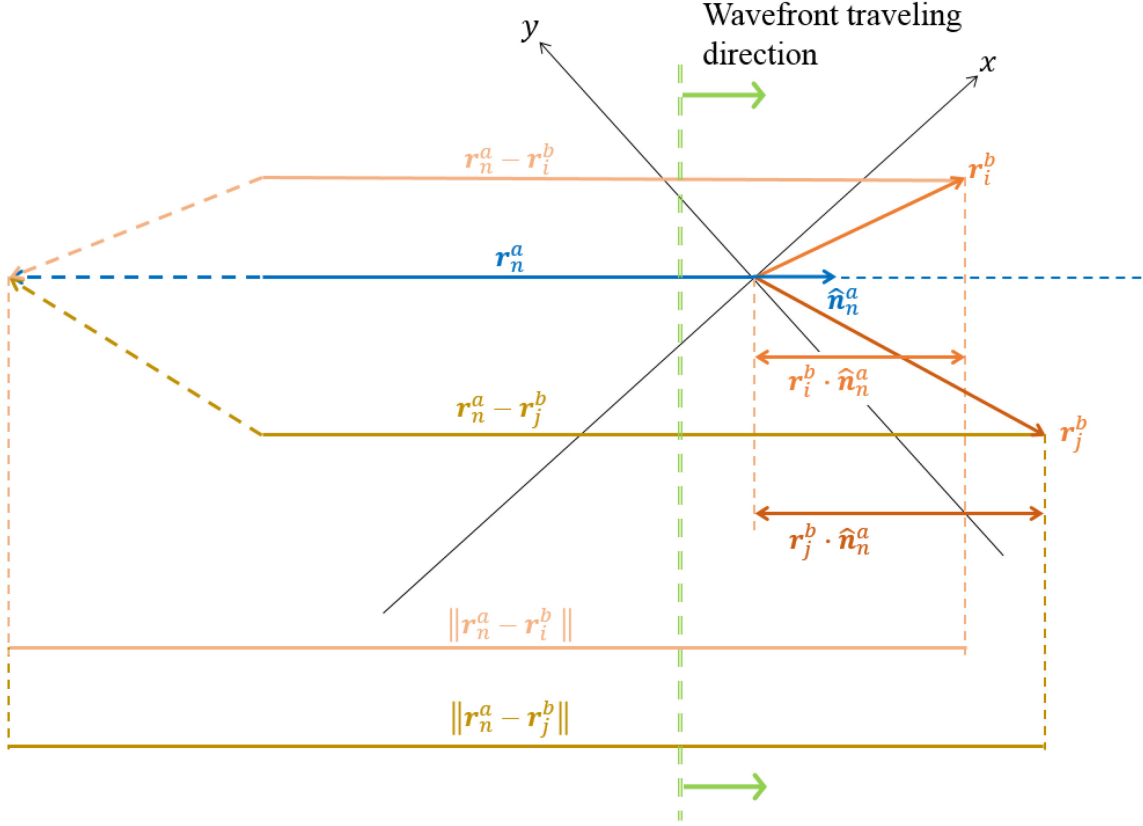
Figure 8: Sensor range difference from the perspective of the transmitted waves

To simplify this expression, the receivers' constellation is shifted so that one sensor is located at zero. In this case, let $\mathbf{r}_j^b = \mathbf{0}$. Equation (3.13) becomes

$$d_{ij} = \left\| \mathbf{r}_n^a - \mathbf{r}_i^b \right\| - \left\| \mathbf{r}_n^a \right\| \tag{3.14}$$

or

$$d_{ij} + \left\| \mathbf{r}_n^a \right\| = \left\| \mathbf{r}_n^a - \mathbf{r}_i^b \right\| \tag{3.15}$$

Squaring Equation (3.15) yields the following:

$$(\mathbf{r}_n^a)^2 + d_{ij}^{\,2} + 2\left\| \mathbf{r}_n^a \right\| d_{ij} = (\mathbf{r}_i^b)^2 - 2\mathbf{r}_i^b \cdot \mathbf{r}_n^a + (\mathbf{r}_n^a)^2$$

$$\left(d_{ij}^{\,2} - (\mathbf{r}_i^b)^2 \right) + \left\| \mathbf{r}_n^a \right\| (2 d_{ij}) + (2\mathbf{r}_i^b) \cdot \mathbf{r}_n^a = 0 \tag{3.16}$$

This equation is valid for all i and j; therefore, it can be generalized with a matrix equation representation as

$$\mathbf{a}_m + \left\|\mathbf{r}_n^a\right\|\mathbf{b}_m + \mathbf{C}_m\mathbf{r}_n^a = 0 \tag{3.17}$$

where $\mathbf{a}_m = \begin{bmatrix} d_{11}^2 - (\mathbf{r}_1^b)^2 \\ d_{21}^2 - (\mathbf{r}_2^b)^2 \\ \vdots \\ d_{M1}^2 - (\mathbf{r}_M^b)^2 \\ d_{12}^2 - (\mathbf{r}_1^b)^2 \\ d_{22}^2 - (\mathbf{r}_2^b)^2 \\ \vdots \\ d_{MM}^2 - (\mathbf{r}_M^b)^2 \end{bmatrix}$, $\mathbf{b}_m = 2\begin{bmatrix} d_{11} \\ d_{21} \\ \vdots \\ d_{M1} \\ d_{12} \\ d_{22} \\ \vdots \\ d_{MM} \end{bmatrix}$, and $\mathbf{C}_m = 2\begin{bmatrix} x_1^b & y_1^b & z_1^b \\ x_2^b & y_2^b & z_2^b \\ \vdots & \vdots & \vdots \\ x_M^b & y_M^b & z_M^b \\ x_1^b & y_1^b & z_1^b \\ x_2^b & y_2^b & z_2^b \\ \vdots & \vdots & \vdots \\ x_M^b & y_M^b & z_M^b \end{bmatrix}$.

Equation (3.17) is linear when either $\mathbf{r}_n^a$ or $\left\|\mathbf{r}_n^a\right\|$ is unknown with the other being given. Although in real world scenarios both $\left\|\mathbf{r}_n^a\right\|$ and $\mathbf{r}_n^a$ are unknown, by using paraxial approximation, $\left\|\mathbf{r}_n^a\right\|$ can be assumed arbitrarily large. This equation can be solved by linear least squares. Recall the least squares best estimate solution to the matrix equation $Ax = b$ is $\hat{x} = (A^T A)^{-1} A^T b$ [28]. Apply this formula to Equation (3.17) as follows:

$$\mathbf{r}_n^a = -\left(\mathbf{C}_m^T\mathbf{C}_m\right)^{-1}\mathbf{C}_m^T\left(\mathbf{a}_m + \left\|\mathbf{r}_n^a\right\|\mathbf{b}_m\right) \tag{3.18}$$

Therefore, the normal direction unit vector of the transmitting wave can then be obtained as the following:

$$\hat{\mathbf{n}}_n^a = -\mathbf{r}_n^a\big/\left\|\mathbf{r}_n^a\right\| = -\left(\mathbf{C}_m^T\mathbf{C}_m\right)^{-1}\mathbf{C}_m^T\left(\mathbf{a}_m\big/\left\|\mathbf{r}_n^a\right\| + \mathbf{b}_m\right) \tag{3.19}$$

33

With the results obtained from paraxial approximation, i.e., $\left\|\mathbf{r}_n^a\right\| \approx \infty \Rightarrow 1/\left\|\mathbf{r}_n^a\right\| \approx 0$,

the estimated bearing vector is the following:

$$\hat{\mathbf{n}}_n^a \approx \lim_{\left\|\mathbf{r}_n^a\right\| \to \infty} \left(-\frac{\mathbf{r}_n^a}{\left\|\mathbf{r}_n^a\right\|}\right) = \left(\mathbf{C}_m^T \mathbf{C}_m\right)^{-1} \mathbf{C}_m^T \mathbf{b}_m \tag{3.20}$$

Equation (3.20) is applied for real world scenarios where transmitters' locations

are unknown but their distances to the region of investigation are far enough to be

estimated as infinitely large. In other words, when $\left\|\mathbf{r}_n^a\right\| \gg \left\|\mathbf{r}_m^b\right\|$, Equation (3.20) is used to

estimate the direction of the incoming waves; however, due to spatial constraints in the

experiment setup discussed in Chapter 4, $\mathbf{r}_n^a$ is not large enough for paraxial

approximation to be valid. In this case, Equation (3.19) is used instead to calculate the

exact direction of the transmitters.

3.5   RF Tomography in Time Domain

3.5.1   Forward Model

Results from Equation (3.12) are used to obtain the estimated time delay for an

object located at $\mathbf{r}_p$. This time delay is

$$\begin{aligned}
\tau_{nmp}(\hat{\mathbf{n}}_n^a, \mathbf{r}_p, \mathbf{r}_m^b) &= \left\{\left\|\mathbf{r}_p - \mathbf{r}_m^b\right\| + \left[\mathbf{r}_p - \mathbf{r}_m^b\right] \cdot \hat{\mathbf{n}}_n^a\right\}/c \\
&= \left\{\left\|\mathbf{r}_p - \mathbf{r}_m^b\right\| + \left[\mathbf{r}_p - \mathbf{r}_m^b\right] \cdot \left[\left(\mathbf{C}_m^T \mathbf{C}_m\right)^{-1} \mathbf{C}_m^T \mathbf{b}_m\right]\right\}/c
\end{aligned} \tag{3.21}$$

Despite being lengthy, Equation (3.21) is significant because it only contains

known quantities. All dependencies on the transmitters' locations have been substituted

by receivers' related terms.

Let $\mathbf{l}_{nmp}[\tau] = A_{pm}r_s\left[\tau - \tau_{nmp}\right]$, Equation (3.12) becomes

$$\mathbf{t}_{nm}[\tau] = A_{mn}r_s[\tau] + \sum_{p=1}^{P}\mathbf{l}_{nmp}v_p$$

$$= A_{mn}r_s[\tau] + \mathbf{s}_{nm}[\tau]$$

(3.22)

where $\mathbf{s}_{nm}[\tau] = \sum_{p=1}^{P}\mathbf{l}_{nmp}[\tau]v_p$, the sum of all matched filtered scattered signals due to P

objects.

Equation (3.22) is the matched filtered total signal received at the mth receiver due

to a wave transmitted by the nth receiver and contains P objects in the scene of

investigation. Figure 9 illustrates this equation by a visual example with a scene of

interest subdivided into six pixels. Only three objects are present at pixels 2, 3, and 5.
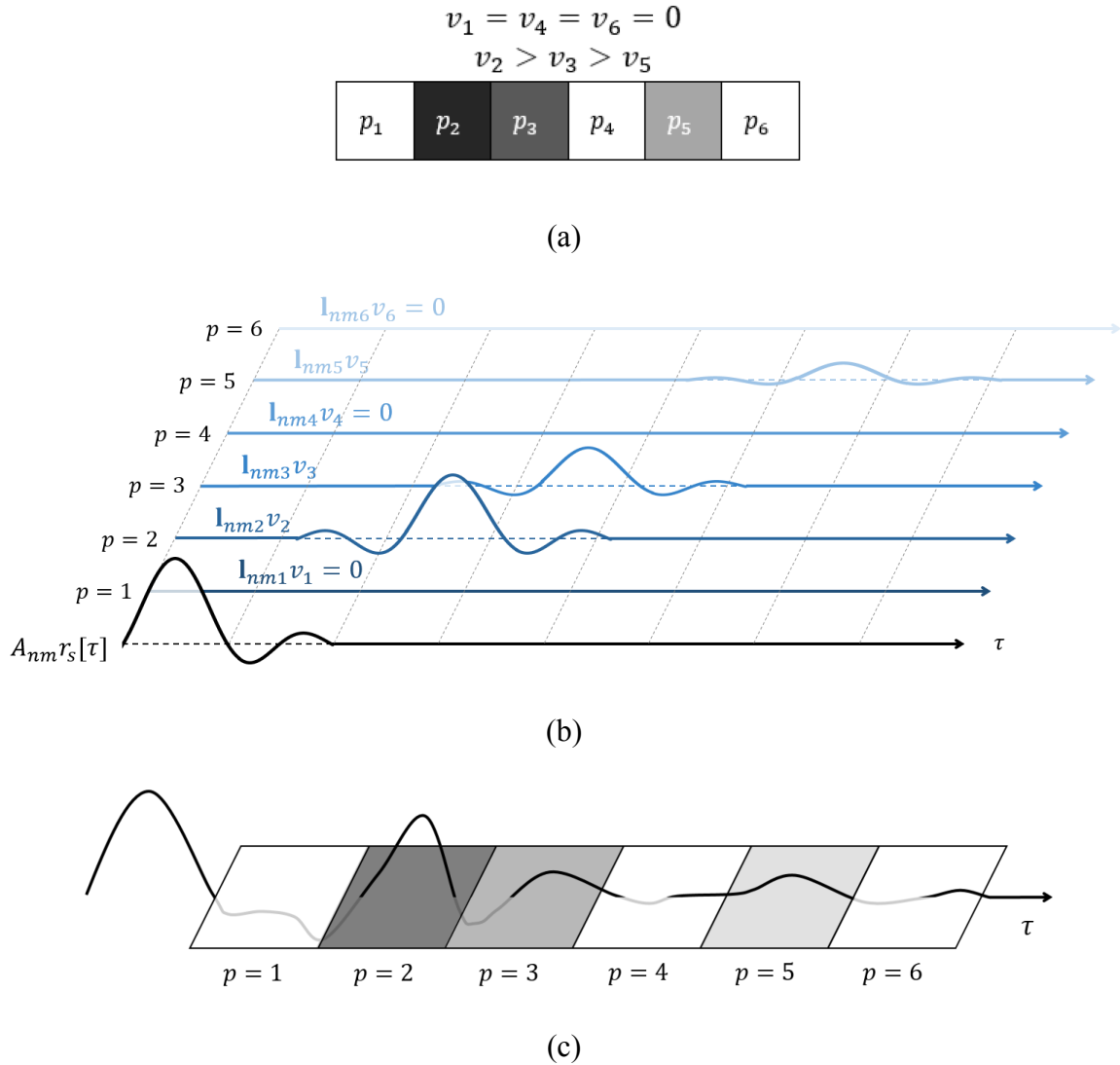
Figure 9: (a) Scene of interest with 6 pixels, three of which contain objects with different reflectivity values. (b) Individualized received signal at the mth receiver due to echoes from three objects in a 6-pixel discretized scene of interest and the direct-path signal from the nth transmitter. (c) Actual received signal, or superposition of all individual received waveforms.

3.5.2 Receiver's Blind Region

For the direct-path signals and echoes to be distinguishable at the receiver's end, the object has to be outside of a certain area with respect to the receiver. In bistatic radar, the object's echoes are obscured by the transmitter's waveform when the bistatic angle $\beta = 180°$, as described in Section 2.5.3; therefore, the blind region of a bistatic radar is a section of the straight line connecting between the transmitter and the receiver. In the case of passive RF tomography, the receiver's blind region is not just a straight line. It is derived as follows:

Let d_r denote the range extension of any transmitter. This quantity is defined as $d_r = \dfrac{c}{B} = c\tau$, where B is the bandwidth of the transmitted waveform and τ is its pulsewidth, as discussed in Chapter 2. For visualization purposes, d_r is the physical length of the transmitted chirp, or the spatial pulse width, measured in meters. Figure 10 illustrates this quantity.
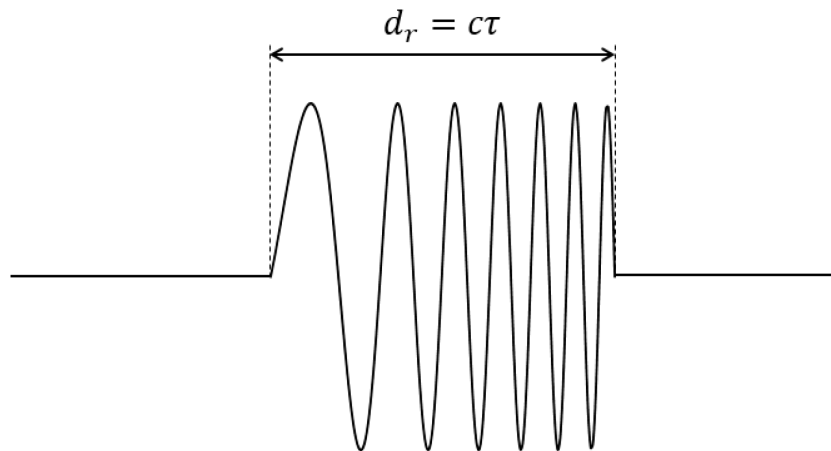

Figure 10: Transmitter's spatial pulse width, $c\tau$

Suppose this pulse is transmitted and scattered by an object from the scene of interest. At the receiver, two waveforms are recorded: The direct path and the scattered signals. There is a time difference between the arrivals of these two waveforms and it is based on the object's location with respect to the receiver and the transmitter. If this time is less than the pulse width, part or all of the scattered signal is obscured by the direct path.

As explained in Chapter 1, recall that the scattered signal $\mathbf{s}_{nm}$ is assumed to be separable from the total received signal $\mathbf{t}_{nm}$. For this assumption to be true, all objects are located so that the wavefront from the nth transmitter and the scattered signal from the pth objects do not overlap at the mth receiver. In other words, the range delay difference between the direct path and scattered signal should be greater than d_r. In terms of positional vectors, this means

$$\left\| \mathbf{r}_n^a - \mathbf{r}_p \right\| + \left\| \mathbf{r}_p - \mathbf{r}_m^b \right\| - \left\| \mathbf{r}_n^a - \mathbf{r}_m^b \right\| > d_r \tag{3.23}$$

Using the paraxial approximation, Inequality (3.23) can be rewritten as

$$\left\| \mathbf{r}_n^a - \mathbf{r}_m^b \right\| + \left(\mathbf{r}_p - \mathbf{r}_m^b \right) \cdot \hat{\mathbf{n}}_n^a + \left\| \mathbf{r}_p - \mathbf{r}_m^b \right\| - \left\| \mathbf{r}_n^a - \mathbf{r}_m^b \right\| > d_r \tag{3.24}$$

or simply

$$\left(\mathbf{r}_p - \mathbf{r}_m^b \right) \cdot \hat{\mathbf{n}}_n^a + \left\| \mathbf{r}_p - \mathbf{r}_m^b \right\| > d_r \tag{3.25}$$

This inequality is visually demonstrated by Figure 11.
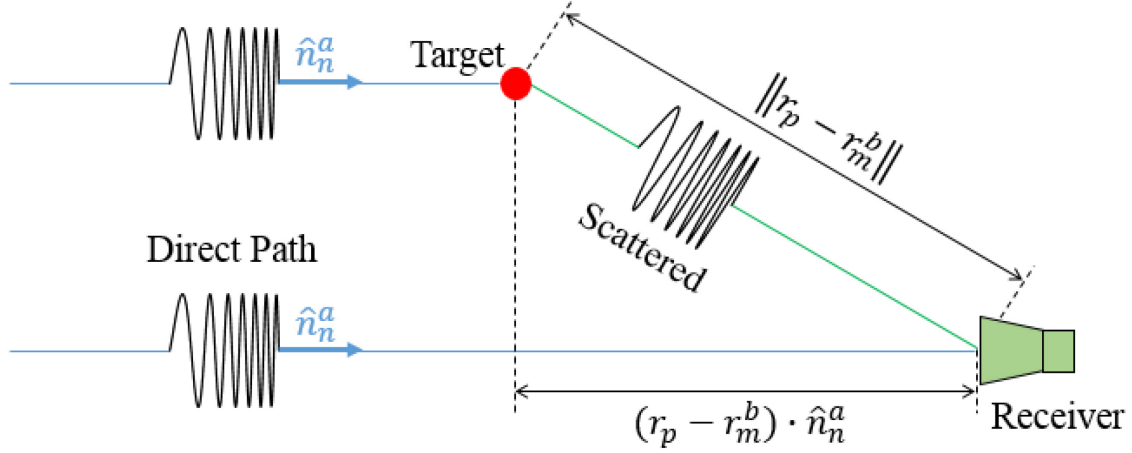
Figure 11: Condition for an object to be out of a receiver's blind region; the range delay difference has to be greater than d_r

Object locations that satisfy the inequality in Equation (3.25) have echoes that are distinguishable from the direct-path signals. To visualize this condition, let $\mathbf{r}_m^b = \mathbf{0}$, which translates the coordinate system's origin to the mth receiver. Equation (3.25) becomes the following:

$$\mathbf{r}_p \cdot \hat{\mathbf{n}}_n^a + \left\| \mathbf{r}_p \right\| > d_r \tag{3.26}$$

Furthermore, to visualize the condition in Equation (3.26), let $\hat{\mathbf{n}}_n^a = \hat{\mathbf{x}}$ and $x_p = \mathbf{r}_p \cdot \hat{\mathbf{x}}$. It is easy to see that $\left\| \mathbf{r}_p \right\|^2 = x_p^2 + y_p^2$. This inequality can be rewritten in the new coordinate system as

$$x_p + \sqrt{x_p^2 + y_p^2} > d_r$$
$$\Rightarrow x_p^2 + y_p^2 > x_p^2 + d_r^2 - 2x_p d_r$$
$$\Rightarrow x_p > \frac{d_r^2 - y_p^2}{2d_r}$$

or

$$x_p > \frac{d_r}{2} - \frac{y_p^2}{2d_r} \qquad (3.27)$$

The plot of Equation (3.27), as shown in Figure 12, is a parabola, the focus of which is at the mth receiver, and the axis of symmetry is along vector $\hat{\mathbf{n}}_n^a$. The blind region of the receiver is the dotted portion enclosed by the parabola. Echoes from objects that are inside this region are not discernable from the direct-path signal originated from the same transmitter.
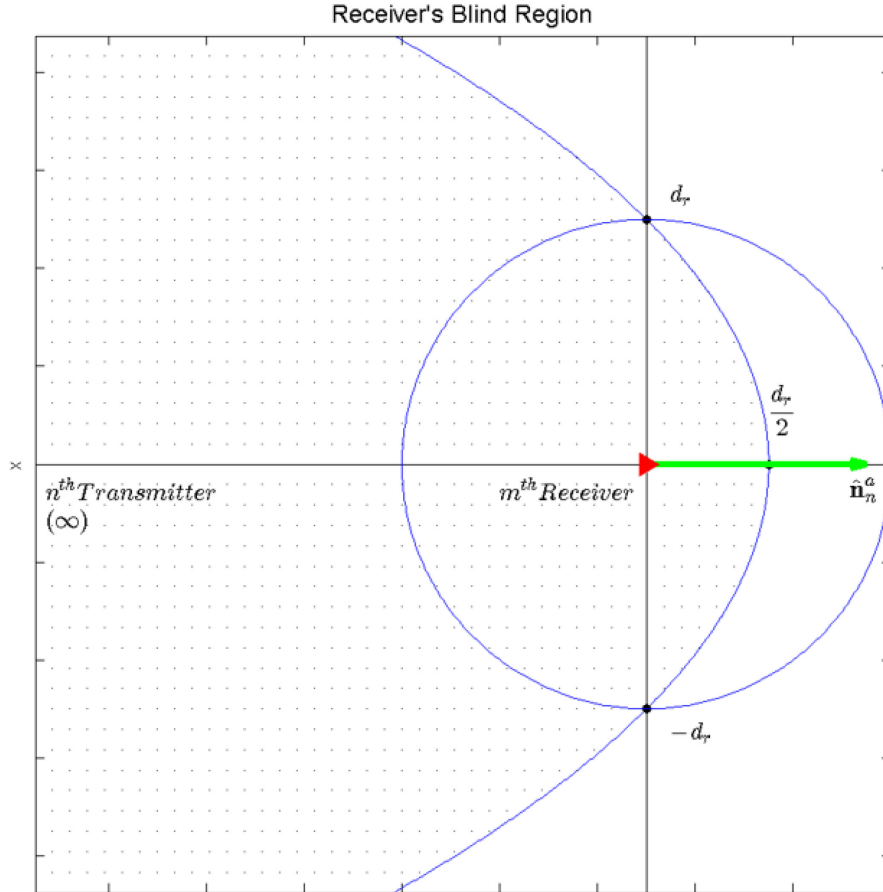
Figure 12: Visualization of the blind spot of each receiver in terms of range resolution of the received signal from a particular transmitter

40

3.5.3 Image Reconstruction

Because the transmitted signals are separable in frequency, their matched filtered echoes recorded at each receiver due to different objects, $\mathbf{l}_{nmp}$, are also separable. This signal is defined as

$$\mathbf{l}_{nmp}[\tau] = \begin{cases} 0, & -K \leq \tau < \tau_{nmp} - T_s \\ A_{pm} r_s[\tau - \tau_{nmp}], & \tau_{nmp} - T_s \leq \tau \leq \tau_{nmp} + T_s \\ 0, & \tau_{nmp} + T_s < \tau \leq +K \end{cases} \qquad (3.28)$$

where τ_{nmp} is the range delay intrinsic to each transmitter, receiver, and object as defined in Equation (3.21).

The vector $\mathbf{l}_{mnp}[\tau]$ is a shifted, or delayed, and scaled version of the correlation sequence $r_s[\tau]$. The shift is equal to τ_{nmp}; thus the support for $\mathbf{l}_{mnp}[\tau]$ is also shifted by τ_{nmp}; furthermore, because the scattered signal from each object due to each transmitter is separable, $\mathbf{l}_{mnp}[\tau]$ is zero everywhere outside of its domain. Figure 13 graphically illustrates one instance of vector $\mathbf{l}_{mnp}[\tau]$. The amplitude of the signal is color coded with solid black being highest and solid white weakest.
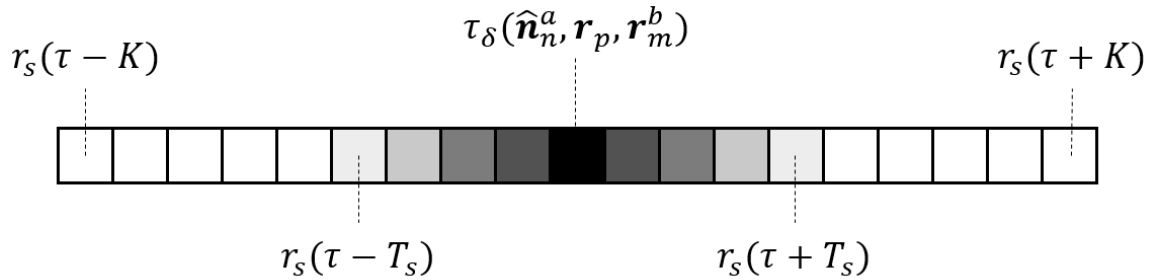

Figure 13: Graphical representation of the matched filtered scattered signal of the pth object due to radiated signal from the nth transmitter at the mth receiver

From Equation (3.22), it is easy to see that

$$\mathbf{s}_{nm} = \mathbf{l}_{nm1}v_1 + \mathbf{l}_{nm2}v_1 + \cdots + \mathbf{l}_{nmP}v_P$$
$$= \mathbf{L}_{nm} \cdot \mathbf{v}$$

(3.29)

where $\mathbf{L}_{nm} = \begin{bmatrix} \mathbf{l}_{mn1} & \mathbf{l}_{mn2} & \mathbf{l}_{mnP} \end{bmatrix}$ and $\mathbf{v} = \begin{bmatrix} v_1 & v_2 & \cdots & v_P \end{bmatrix}^T$.

The generalized expression that relates collected data is therefore

$$\underbrace{\begin{bmatrix} \mathbf{s}_{11} \\ \mathbf{s}_{12} \\ \vdots \\ \mathbf{s}_{1M} \\ \mathbf{s}_{21} \\ \mathbf{s}_{22} \\ \vdots \\ \mathbf{s}_{NM} \end{bmatrix}}_{\mathbf{s}} = \underbrace{\begin{bmatrix} \mathbf{l}_{111} & \mathbf{l}_{112} & \cdots & \mathbf{l}_{11P} \\ \mathbf{l}_{121} & \mathbf{l}_{122} & \cdots & \mathbf{l}_{11P} \\ \vdots & \vdots & \ddots & \vdots \\ \mathbf{l}_{211} & \mathbf{l}_{212} & \cdots & \mathbf{l}_{21P} \\ \mathbf{l}_{221} & \mathbf{l}_{222} & \cdots & \mathbf{l}_{22P} \\ \vdots & \vdots & \ddots & \vdots \\ \mathbf{l}_{NM1} & \mathbf{l}_{NM2} & \cdots & \mathbf{l}_{NMP} \end{bmatrix}}_{\mathbf{L}} \cdot \underbrace{\begin{bmatrix} v_1 \\ v_2 \\ \vdots \\ v_P \end{bmatrix}}_{\mathbf{v}}$$

(3.30)

or simply

$$\mathbf{s} = \mathbf{L} \cdot \mathbf{v}$$

(3.31)

To visualize Equation (3.31), consider an example scene layout in Figure 14 with six isotropic objects located in six adjacent pixels. Each object has a reflectivity of v_i where $i = 1, 2, \ldots, 6$.
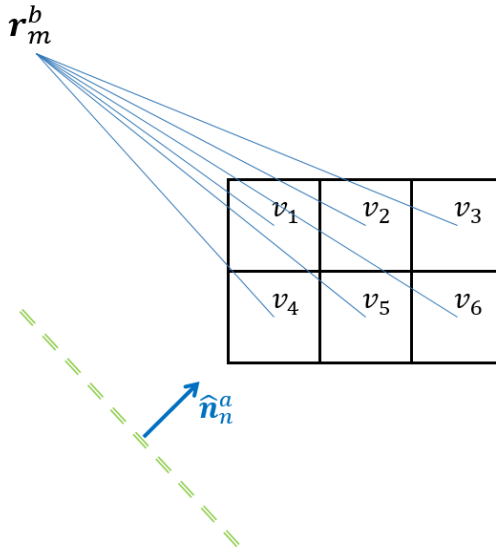
Figure 14: Example layout of a scene of interest with six objects

Figure 15 illustrates the tomographic model defined by Equation (3.31) of this scene. Each object has a different range delay with respect to the mth receiver.
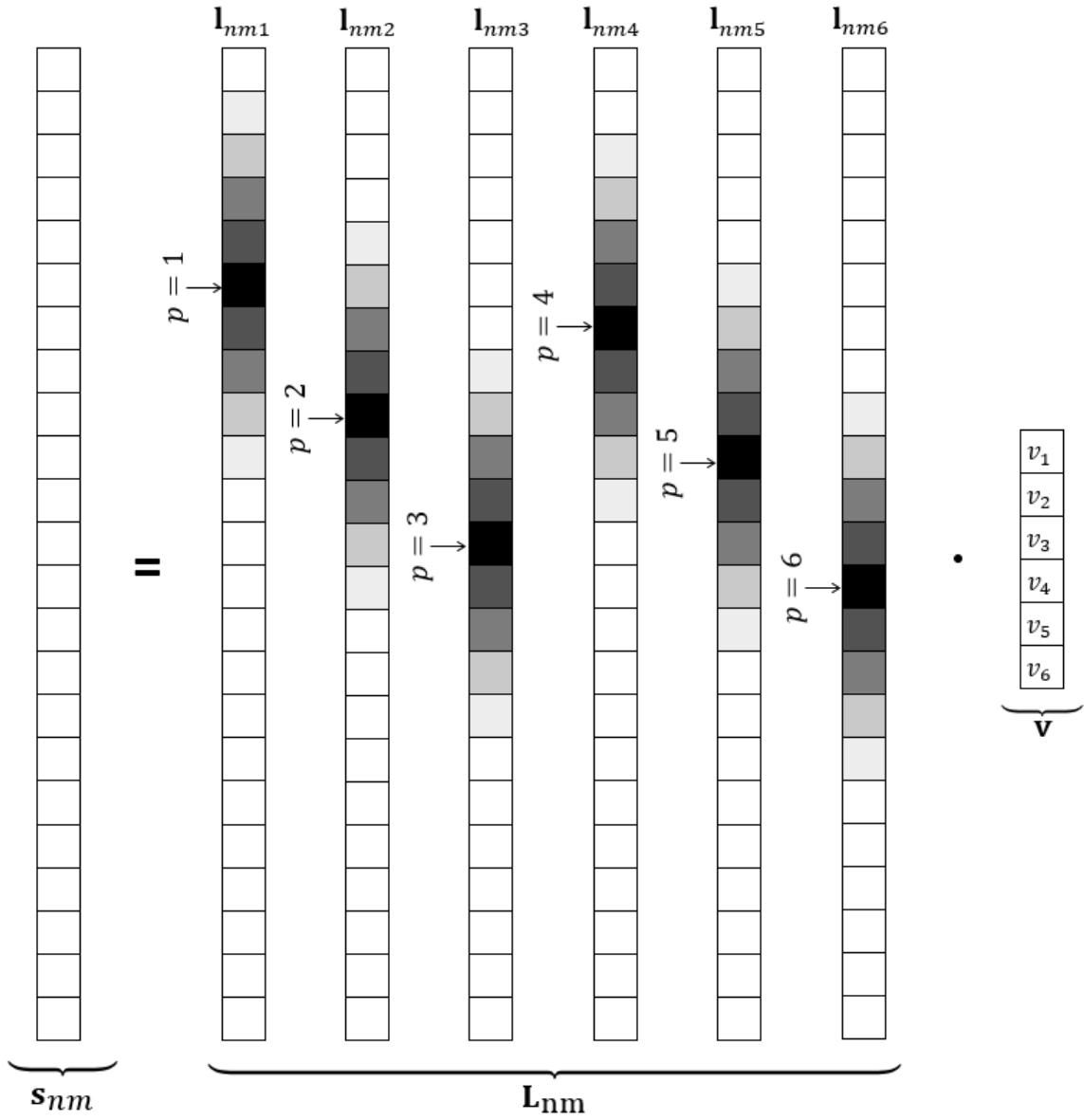
Figure 15: Visualization of the forward tomographic model. Bolder squares denote stronger magnitudes.

Vector $\mathbf{v} = \begin{bmatrix} v_1 & v_2 & \cdots & v_P \end{bmatrix}^T$ represents the unknowns of the imaging problem. It can be obtained from Equation (3.31) by means of matrix inversion. Matrix $\mathbf{L}$, however, may not be invertible; therefore, another method to obtain $\mathbf{v}$ is proposed as follows:

Consider a simple case where one object is present in the area of interest. In other words, let $v_1 = 1$ and $v_n = 0$ with $\forall n \neq 1$. Equation (3.30) becomes the following:

$$\mathbf{s} = \mathbf{l}_{nm1}v_1 + \underbrace{\mathbf{l}_{nm2}v_1 + \cdots + \mathbf{l}_{nmP}v_P}_{0} = \mathbf{l}_{nm1}v_1 \qquad (3.32)$$

It is easier to derive a filter that maximizes the signal to noise ratio (SNR) when applied to vector $\mathbf{s}$ than to directly solve for v_1. This filter is similar to a matched filter which uses $\mathbf{l}_{nm1}$ as the reference to detect if there is an object present at pixel $p = 1$. If there is no object, the total recorded signal, $\mathbf{s}$, does not contain the reference pattern of $\mathbf{l}_{nm1}$, and, therefore, the output of the filter is zero. The derivation is as follows:

Let the unknown filter be a row vector $\mathbf{w}^H$. The imaging problem becomes a maximization of the value $y_1 = \mathbf{w}^H \cdot \mathbf{s}$, which will be used for image reconstruction instead of v_1. Because $\mathbf{s}$ may contain noise, it can be rewritten as $\mathbf{s} = \mathbf{l}_{nm1} + \mathbf{m}_{nm1}$ where $\mathbf{m}_{nm1}$ is the white Gaussian noise portion of signal $\mathbf{s}$ corresponding to $\mathbf{l}_{nm1}$. This noise has zero mean and a variance of $\sigma^2\mathbf{I}$ where $\mathbf{I}$ is an identity matrix.

The SNR of $\mathbf{s}$ after applying the filter $\mathbf{w}^H$ is

$$SNR = \mathrm{E}\left[\frac{\left| \mathbf{w}^H \mathbf{l}_{nm1} \right|^2}{\left| \mathbf{w}^H \mathbf{m}_{nm1} \right|^2} \right] \qquad (3.33)$$

where $E[x(t)]$ denotes the expected value of a sequence $x(t)$.

Expanding Equation (3.33) gives the following:

$$SNR = \frac{E\left[\mathbf{w}^H \mathbf{l}_{nm1} \mathbf{l}_{nm1}^H \mathbf{w}\right]}{E\left[\mathbf{w}^H \mathbf{m}_{nm1} \mathbf{m}_{nm1}^H \mathbf{w}\right]}$$

(3.34)

Only the denominator of the SNR contains a random sequence $\mathbf{m}_{nm1}$. Other terms are deterministic; therefore,

$$SNR = \frac{\mathbf{w}^H \mathbf{l}_{nm1} \mathbf{l}_{nm1}^H \mathbf{w}}{\mathbf{w}^H E\left[\mathbf{m}_{nm1} \mathbf{m}_{nm1}^H\right] \mathbf{w}}$$

(3.35)

Note that $Var[\mathbf{m}_{nm1}] = E\left[\mathbf{m}_{nm1}^2\right] - \left(E[\mathbf{m}_{nm1}]\right)^2 = E\left[\mathbf{m}_{nm1} \mathbf{m}_{nm1}^H\right] = \sigma^2 \mathbf{I}$. The SNR becomes

$$SNR = \frac{\mathbf{w}^H \mathbf{l}_{nm1} \mathbf{l}_{nm1}^H \mathbf{w}}{\mathbf{w}^H \sigma^2 \mathbf{I} \mathbf{w}} = \frac{\left|\mathbf{w}^H \mathbf{l}_{nm1}\right|^2}{\sigma^2 \mathbf{w}^H \mathbf{w}} = k \left|\mathbf{w}^H \mathbf{l}_{nm1}\right|^2$$

(3.36)

Because $\mathbf{w}$ is a column vector, $\mathbf{w}^H \mathbf{w}$ is a constant. Equation (3.36) can be rewritten as

$$SNR = k \left|\mathbf{w}^H \mathbf{l}_{nm1}\right|^2$$

(3.37)

where $k = \dfrac{1}{\sigma^2 \mathbf{w}^H \mathbf{w}}$. To determine $\mathbf{w}$ to maximize the SNR, the Cauchy-Schwarz Inequality can be applied as follows:

$$\left|\mathbf{w}^H \mathbf{l}_{nm1}\right|^2 \le \left|\mathbf{w}^H\right|^2 \cdot \left|\mathbf{l}_{nm1}\right|^2$$

(3.38)

It is easy to see that $\left|\mathbf{w}^H\right|^2 = \left|\mathbf{w}\right|^2$; therefore, the inequality in Equation (3.38) becomes

$$\left|\mathbf{w}^H \mathbf{l}_{nm1}\right|^2 \leq \left|\mathbf{w}\right|^2 \cdot \left|\mathbf{l}_{nm1}\right|^2 \tag{3.39}$$

The SNR is maximized when $\mathbf{w} = \mathbf{l}_{nm1}$, according to Cauchy-Schwarz. The value of y_1 is thus estimated by $y_1 = \mathbf{l}_{nm1}^H \cdot \mathbf{s}$. Expanding this result to the full area of investigation that contains P objects, a general expression can be obtained as follows:

$$\mathbf{y} = \mathbf{L}^H \cdot \mathbf{s} \tag{3.40}$$

where $\mathbf{y} = \begin{bmatrix} y_1 \\ y_2 \\ \vdots \\ y_P \end{bmatrix}$.

Image reconstruction is accomplished through $\mathbf{y}$ as a substitute for vector $\mathbf{v}$. The same result can be achieved by means of matrix pseudoinverse of Equation (3.31) using the back-propagation method [8] [29].

3.6   Summary

The methodology presented in this chapter is the foundation for a hardware and software implementation as proof of concept of passive RF tomography. The hardware system design and its specifications, as well as the signal processing procedure for image formation are explained in detail in the next chapter, along with the obtained results.

IV. Hardware Implementation, Results, and Analysis

This chapter provides a proof of concept for passive RF tomography by means of hardware implementation and experiment. First, an overview of the specifications of the test system is discussed. This system is used to capture and process data of the experiment, which is described next. Recorded data are conditioned and demodulated to baseband for subsequent processing. These steps are described before results obtained from the experiment are explained and analyzed.

4.1   Hardware Implementation

The hardware experimental setup consists of four independent transmitters and four independent receivers. Each transmitter radiates different and arbitrarily generated waveforms. Each waveform is separated in frequency and time, according to the assumptions made in Chapter 1. All receivers are coherent and share the same reference clock. Each transmitter and receiver channel is connected to an antenna with a 10 dBi gain. The maximum length of the rugged low-loss connecting cables is 75 feet. For complete specifications of the test system, refer to Table 1. All operations, including waveform generation, signal conversion, data recording, processing, and image reconstruction are user-controlled through a high-power central computer workstation running MATLAB. Other attached instrumentation and equipment such as the pulse generator, Rubidium oscillator, signal generator (SigGen), local oscillator (LO), and power supply (PSU) are also controlled through MATLAB over TCP/IP. AC power input to the system is protected by an uninterruptible power supply (UPS) unit. The rack-mounted equipment is shown in Figure 16.
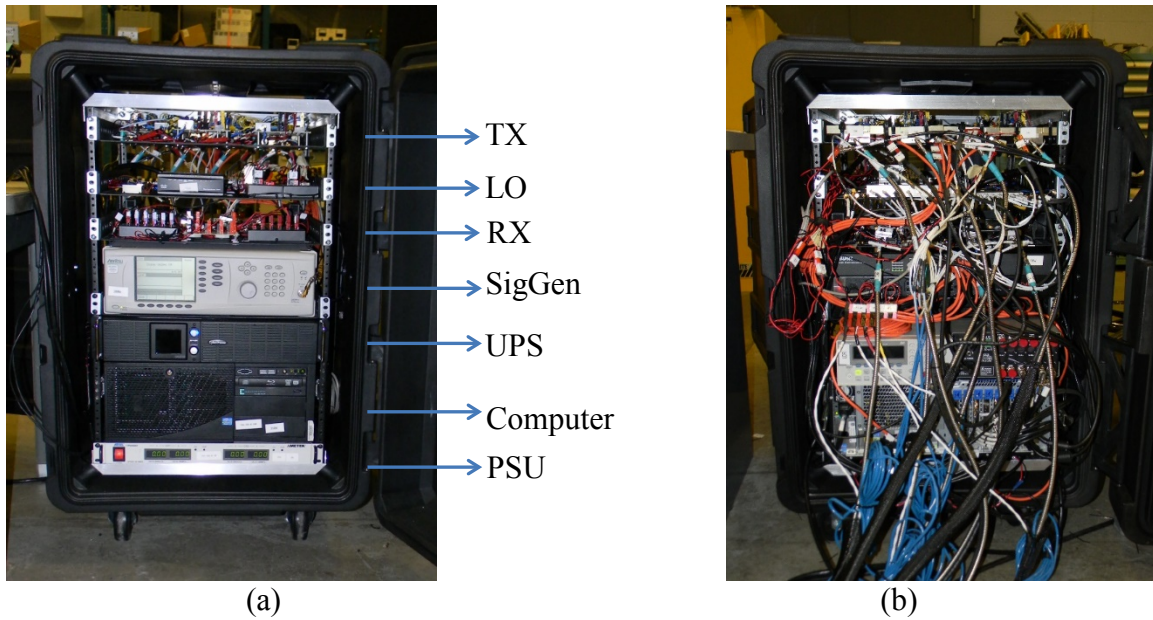
Figure 16: Photos of the test system: (a) front and (b) back

4.1.1 General Operation

Although this experiment is meant to prove the concept of passive RF tomography, it is more feasible to actively transmit suitable signals that conform to the assumptions discussed in Chapter 1; however, the passive mode of operation can still be realized by ignoring the knowledge of the transmitters and their generated waveforms at the signal processing steps.

The operation of the test system is as follows. Signals generated from the 4-channel advanced waveform generator (AWG) are transmitted to the input of each channel of the transmitter. This signal has a bandwidth of 400 MHz with a starting frequency near DC. This bandwidth yields a bistatic range resolution of approximately

$d_r = \dfrac{c}{2B\cos\beta} \approx 0.375\cos\beta$ m. Before being radiated through an antenna attached at the

end of the transmission line, the signal first goes through a digitally controlled attenuator for the purpose of adaptive adjustment of the dynamic range. This feature allows the output power of each channel to be equal and independent of the length of RF cables connecting the antennas to the rest of the equipment mounted in a rack at the control station. It also maximizes dynamic range of the received signals to account for weak incoming waveforms (in the −80 dBm range) due to either distance of the transmitters or low transmission power.

Next, the signal is low-pass filtered then modulated to the S-band at 2 GHz. This is accomplished by a mixer which produces a new output signal by adding the following frequencies from the input: The baseband and the LO signal operating at 2 GHz. This upconverted signal is band-pass filtered and mixed with another LO at 8 GHz to reach the desired operating frequency in the X-band. The two-stage mixing process was chosen to make this test system more flexible and adaptable to a wide range of operating frequencies. This flexibility is accomplished simply by tuning the LO of the second mixer. To achieve the average output power of 1 W (30 dBm), this signal is amplified twice. The first amplification stage is right before the long RF cable (up to 75 feet) attached to the radiating element. At this stage, the transmitted signal receives gain by a high-power amplifier (HPA). The second amplification is achieved by applying the same HPA at the end of the RF cable and before the antenna.

Similarly, each of the four coherent receivers captures incoming waveforms through an antenna with the same specifications as those of transmitters. The output of this antenna first passes through a digitally controlled attenuator to equalize the dynamic range among all four channels. This signal is amplified by a low-noise amplifier (LNA)

50

close to the antenna. A RF cable, up to 75 ft in length, conducts this signal back to the equipment rack, where it is amplified again with an identical LNA. The signal is filtered, down-converted to the S-band using a mixer with an LO signal at 6 GHz, and then mixed with a second LO at 2 GHz to arrive at baseband. At this stage, it is amplified one last time, low-pass filtered, and transcoded by an analog-to-digital converter (ADC) for later processing. For a full block diagram, refer to Figure 17. This diagram divides the system into three distinct portions: The computer, equipment rack, and antennas. The first part of the system is the *brain* which contains the DAC and ADC, the software (MATLAB) to control all equipment and operations, and storage for recording data. The second is the enclosure of all active and passive components which translate outgoing and incoming signals to and from the computer. The last components in the transmission lines are located close to the transmitter and receiver antennas, along with their accompanying amplifiers and digital attenuators.

Table 1: Hardware specifications of X-band test system

| Specification	Value
Number of Transmitters	4
Number of Receivers	4
Frequency of Operation	8.2-10.6 GHz
Bandwidth	500 MHz
Average Output Power	30 dBm (1 W) Typical
Antenna Gain	10 dBi
Advanced Waveform Generator Speed	1.2 GS/s
Analog to Digital Converter Speed	1.2 GS/s at 8-bit resolution
Noise Floor	−84 dBm
Maximum Received Power	+25 dBm (with attenuation)
Range (0 dB RCS)	4 to 200 m (calculated)
Cable Length (to Antenna)	25 - 50 - 75 ft
Pulse Repetition Frequency	Up to continuous streaming
Synchronization	Rubidium clock 10 MHz
DDR3 Memory Capacity	256 GB
Data Recording Speed	1.2 GB/s
Storage Capacity	6 TB
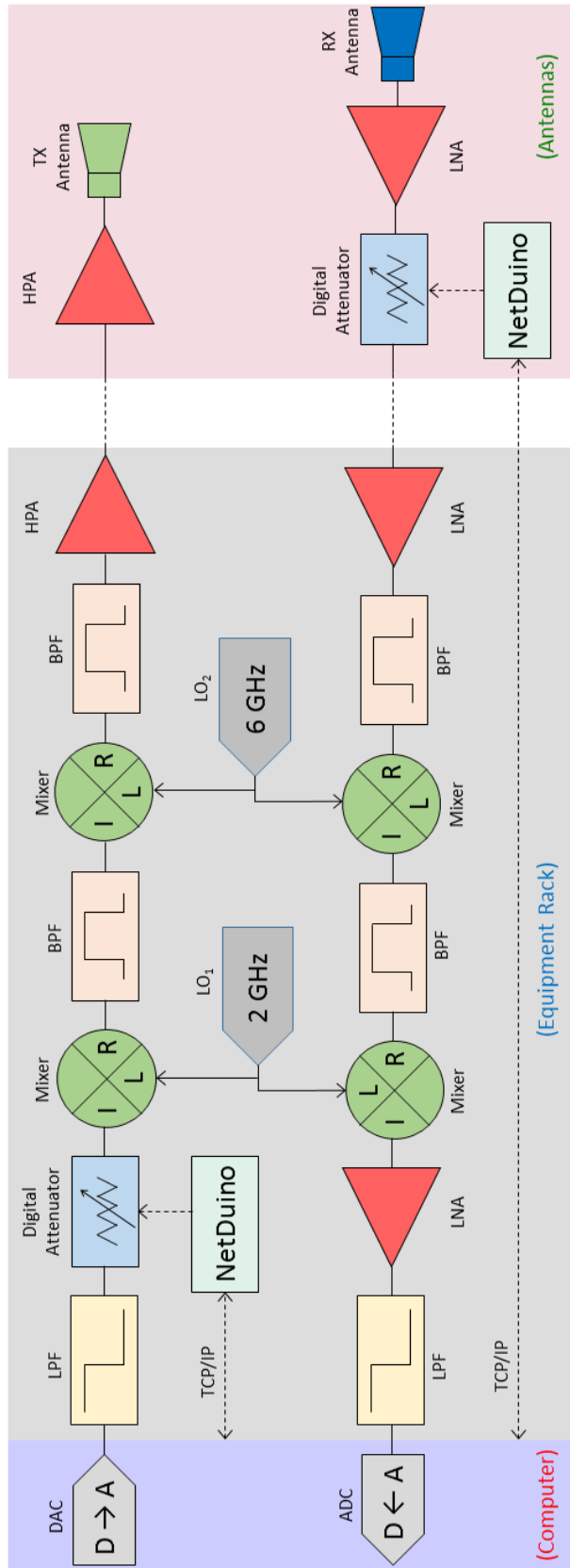
Figure 17: Full system block diagram of the X-band test system for one transmit and one receive channels

4.1.2 Adaptive Adjustment of the Dynamic Range

For the purpose of regulating the output and input power of the transmitted and received signals, a digitally- controlled attenuator is installed on each channel. On the transmitters' side, the attenuators are located at the baseband, whereas the receivers' attenuators are at the X-band, next to the antennas. Each attenuator is connected to a NetDuino through its Digital I/O ports. The transmitters' and receivers' attenuators have different levels as well as steps of attenuation. This variation results in different number of control bits used in each channel. Depending on the number of the control bits, an identical number of pins are used to define the attenuation level for each attenuator. The maximum levels of attenuation are 65 dB and 42 dB for the TX and RX sides, respectively. The NetDuino communicates with the central computer's software MATLAB through TCP/IP. Figure 18 details the schematic of a digital attenuator setup.

Ideally, the system should be able to automatically detect the signal levels and adjust the amount of attenuation accordingly to equalize the transmitted and received waveforms. This feature helps maximizing the SNR of both outgoing and incoming signals; however, due to time constraints of the project, this goal was not fully accomplished. Instead, the attenuation levels are manually tuned for each receiver channel during the experiment. Adjusting attenuation values is done by observing the clipping of received waveforms and adjusting the degree of attenuation appropriately to eliminate signal compression. This step is the precursor of the next procedure, signal conditioning, which prepares the recorded data for image reconstruction.
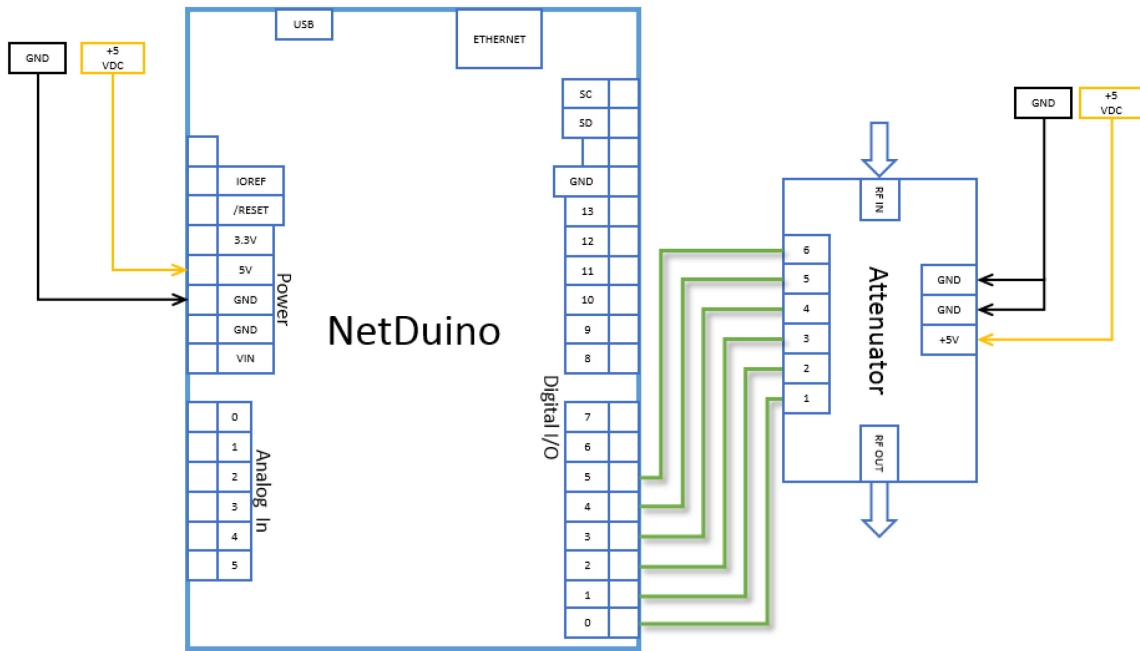
Figure 18: Schematic of one digitally controlled attenuator

4.2 Signal Conditioning

Incoming signals recorded at the four receivers are not ready for signal processing due to possible misalignment with respect to each other; furthermore, the recorded waveforms have to be demodulated to reduce the bandwidth, sample size, and to obtain in-phase (I) and quadrature (Q) information.

4.2.1 Data Alignment

The received waveforms from different sensors are not always aligned even though they share the same reference clock. This effect could be due to inaccuracies in the DAC module which may result in a small shift, usually one to three samples, among the captured data series. Additionally, the high sampling rate of 1.2 GS/s may exacerbate

the errors and increase the variance of the shifts. Because reconstruction relies on the accuracy of the TDOA, it is crucial to have all incoming waveforms at all four receivers aligned for an accurate image to be formed.

A simple solution to this problem is realignment of data from each receiver so that they all line up at the first pulse. Because this experiment is meant for passive mode of operation, transmitted pulses are not available for referencing; instead, the first received pulse is used as reference for lagging pulses. Figure 19 illustrates a simple case of three misaligned captured waveforms and how they are corrected using the first pulse as reference.
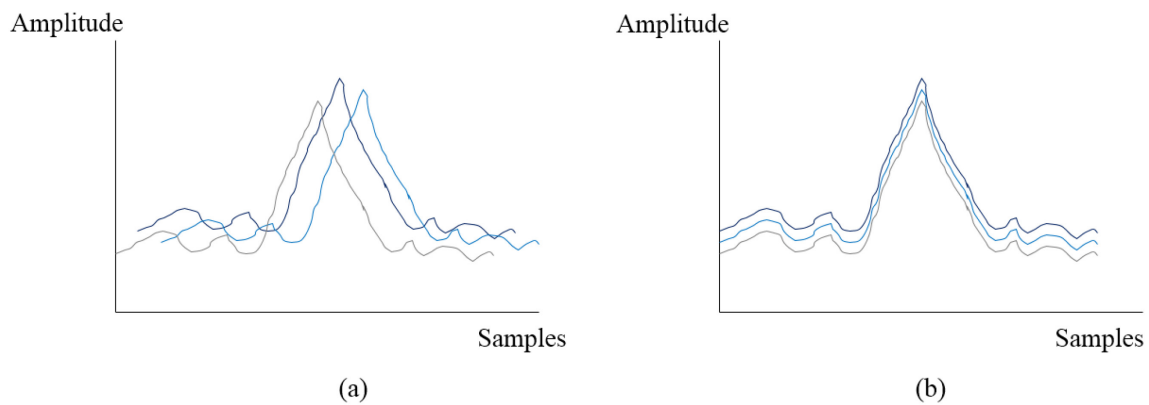

Figure 19: (a) Misaligned signals from different receivers, (b) Realigned data

4.2.2 Digital Demodulation and Resampling

After realignment, every recorded waveform needs demodulating for subsequent processing. Because received data are real, their Fourier transforms are symmetric in the frequency domain. This symmetry makes it possible to discard the negative frequency portion of the signal spectrum without loss of information. After filtering out this negative frequency component, the remaining positive part is demodulated to baseband

56

with center frequency at zero. With the inverse FFT, I and Q data are recovered. This process is illustrated in Figure 20.
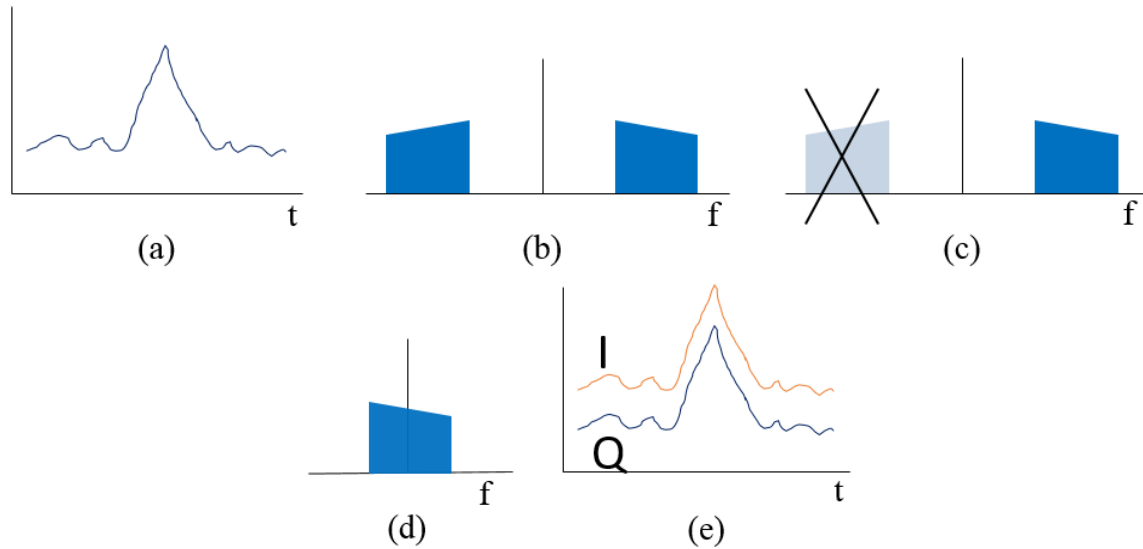

Figure 20: Digital demodulation. Real recorded signal (a) and its symmetric frequency spectrum (b). The negative frequency part (c) can be removed without loss of information. Signal is demodulated to baseband (d) and its inverse Fourier transform (e)

4.3   Experiment Setup

The experiment is based on the theory, established in Chapter 3, in which distributed receivers are scattered about the scene of interest. There are four transmitters and four receivers. Although information about transmitters' waveforms is ignored in the signal processing steps as described in Section 4.1, the waveforms are controlled to properly fit the necessary conditions laid out in the assumptions.

The transmitter and receiver constellation are set up as follows: On an 8×8 m square grid, the transmitters' antennas are placed at the vertices and the receivers' antennas at the midpoints of the sides. They are labeled TX_n for the nth transmitter channel and RX_m for the mth receiver channel. All antennas are raised approximately 1.5

57

meters off the ground by tripods. The approximated main beam of each antenna is pointed towards the center of the square grid, and the grid center is assigned to be the center of the coordinate system. Due to the time and budget constraints of this project, the effect of antenna pattern is not studied in this thesis.

The transmitters' antennas are located at coordinates $(-4, -4)$, $(-4, 0)$, $(4, 4)$, and $(4, -4)$ for TX_1, TX_2, TX_3, and TX_4, respectively. Similarly, the positions of receivers' antennas are $(-4, 0)$, $(0, 4)$, $(4, 0)$, and $(0, -4)$ for RX_1, RX_2, RX_3, and RX_4, respectively. Within this square is a 5×5 m discretized area of interest where possible objects are located. A 12-inch (30 cm) diameter test object is placed inside this imaging grid at coordinates $(-1, -1)$. It is also approximately raised 1.5 m off ground by a non-reflective stand. This geometry is illustrated in Figure 21.
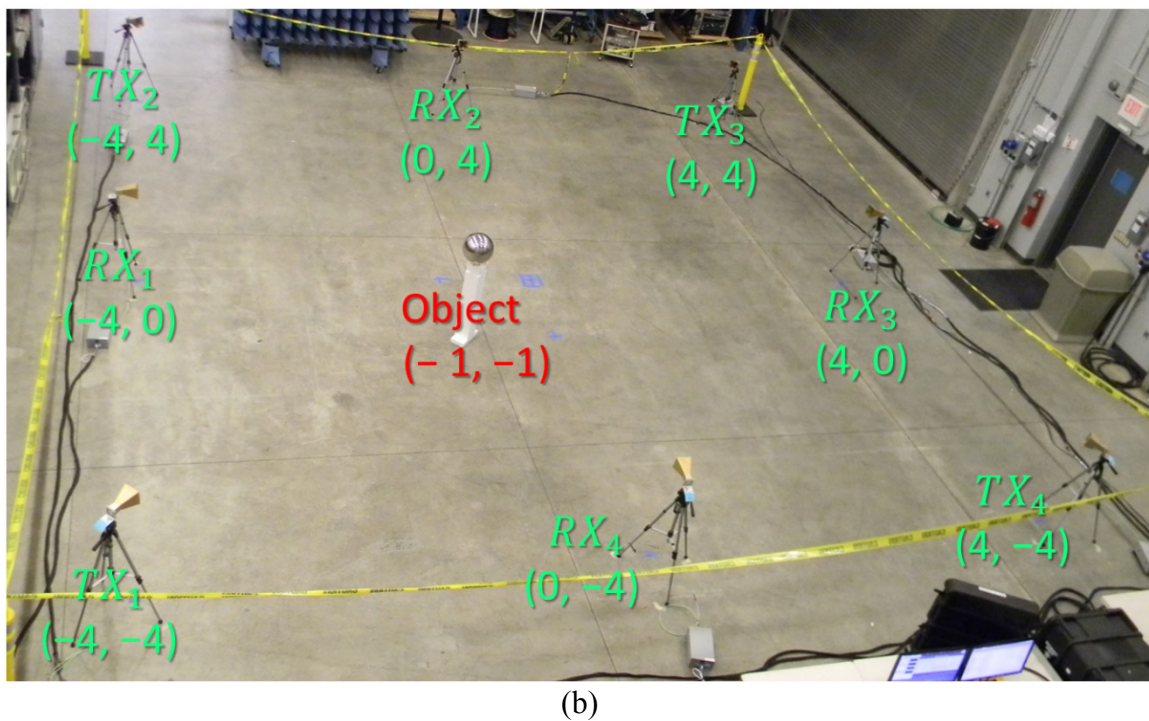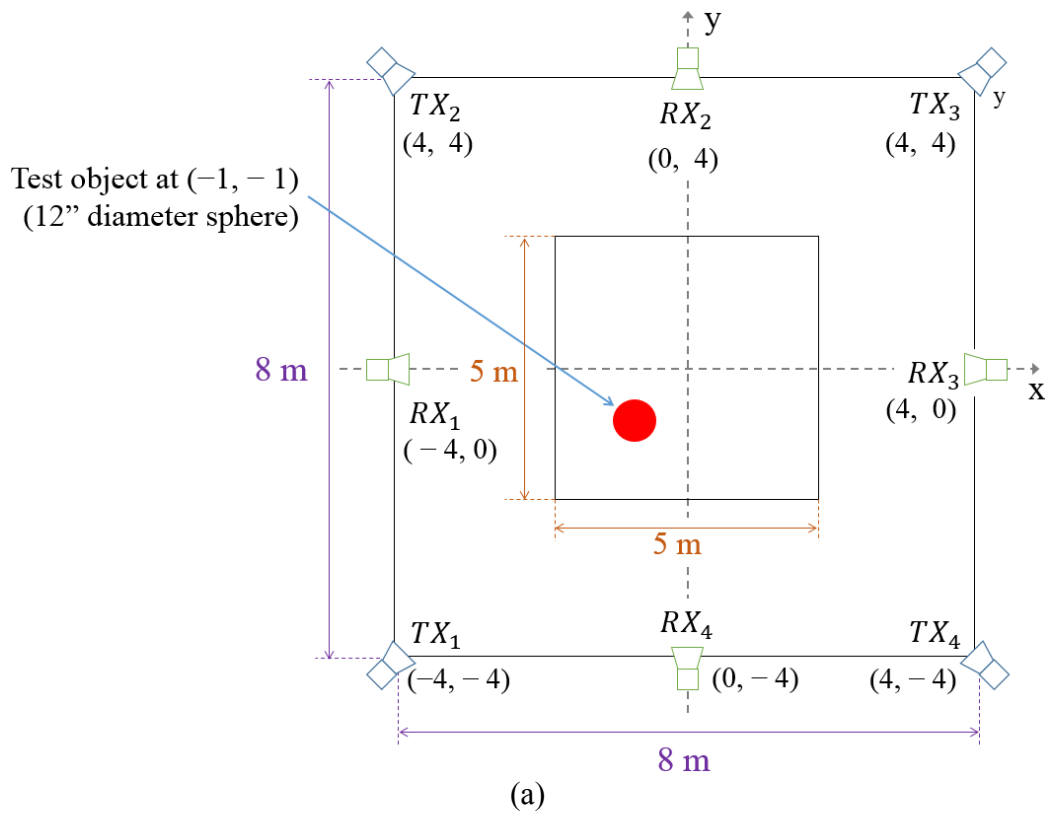
Figure 21: Experiment setup. (a) Geometry (not drawn to scale). (b) Overhead view of

actual layout

It is important to note that although the theory calls for transmitters infinitely far away from receivers and objects, spatial constraints of the testing area as well as cable length do not allow for such conditions; therefore, the geometry of the experiment has to limit the distance of the transmitters, thus making them a finite quantity. This setup, however, does not invalidate the theory developed in Chapter 3. Instead of using $\left\| \mathbf{r}_n^a \right\| = \infty$ for the source localization to estimate the direction of incoming waves from each transmitter, $\hat{\mathbf{n}}_n^a$, it can be calculated directly by applying the known distance $\left\| \mathbf{r}_n^a \right\|$ per each transmitter to Equation (3.19). This is the only difference in the theory and experiment. All subsequent signal processing steps and RF tomographic image reconstruction follow the exact theoretical procedure discussed in Chapter 3.

4.4   Results and Analysis

After data acquisition and signal conditioning, image reconstruction can take place using the bottom line expression from Equation (3.40). When **y** is solved, the tomographic image is reconstructed as follows: Each element of **y** represents the reflectivity of each pixel in the discretized imaging region. Because this area is a square grid, the pixels are rearranged in such a way that their reflectivity values are concatenated in one vector, **y**. The form of this vector is similar to the example in Figure 15.

To better understand the tomographic image obtained from this experiment, the process of reconstruction can be divided to multiple steps. In each step, a transmitter and receiver pair returns a possible set of points where the object is located. This is called the isorange contour, as discussed in Section 2.5. Because there is one object, all contours intersect at a single point at the object location. This procedure is repeated until the

number of pairs of TX-RX is exhausted. Each image is plotted with a dynamic range of 10 dB, as shown in Figure 22 through 27.

Results from the TX_1-RX_1 pair show the isorange contour, which is an ellipse with foci located at the first transmitter and receiver. Figure 22 clearly shows how the isorange contour matches the theory of bistatic radar, demonstrated in Figure 3. This ellipse visibly passes through the point $(-1, -1)$ where the object is present. Additionally, from this figure, the range resolution can be determined. It is equal to the thickness of the isorange contour and can be measured at approximately 0.4 m. This value matches that of the theoretical range resolution of a pulse having the 400 MHz bandwidth calculated in Section 4.1.1. with an estimated error of 10%. The object location and the TX and RX locations are manually overlaid for easier visualization.

Because the experiment was conducted indoors with multiple clutters, background subtraction was employed to remove as much undesired effects from clutters as possible. As the name implies, the process of background subtraction involves using a set of data taken without the object as the background reference. In an attempt to remove the clutter, this reference is then subtracted from the data set that includes the. To further enhance the SNR of the final image, gating was also applied to the data after the background was removed. This action discards echoes beyond a certain distance from each antenna so that only scattered signals from the scene of interest are used for imaging. Anything outside of this region is truncated.
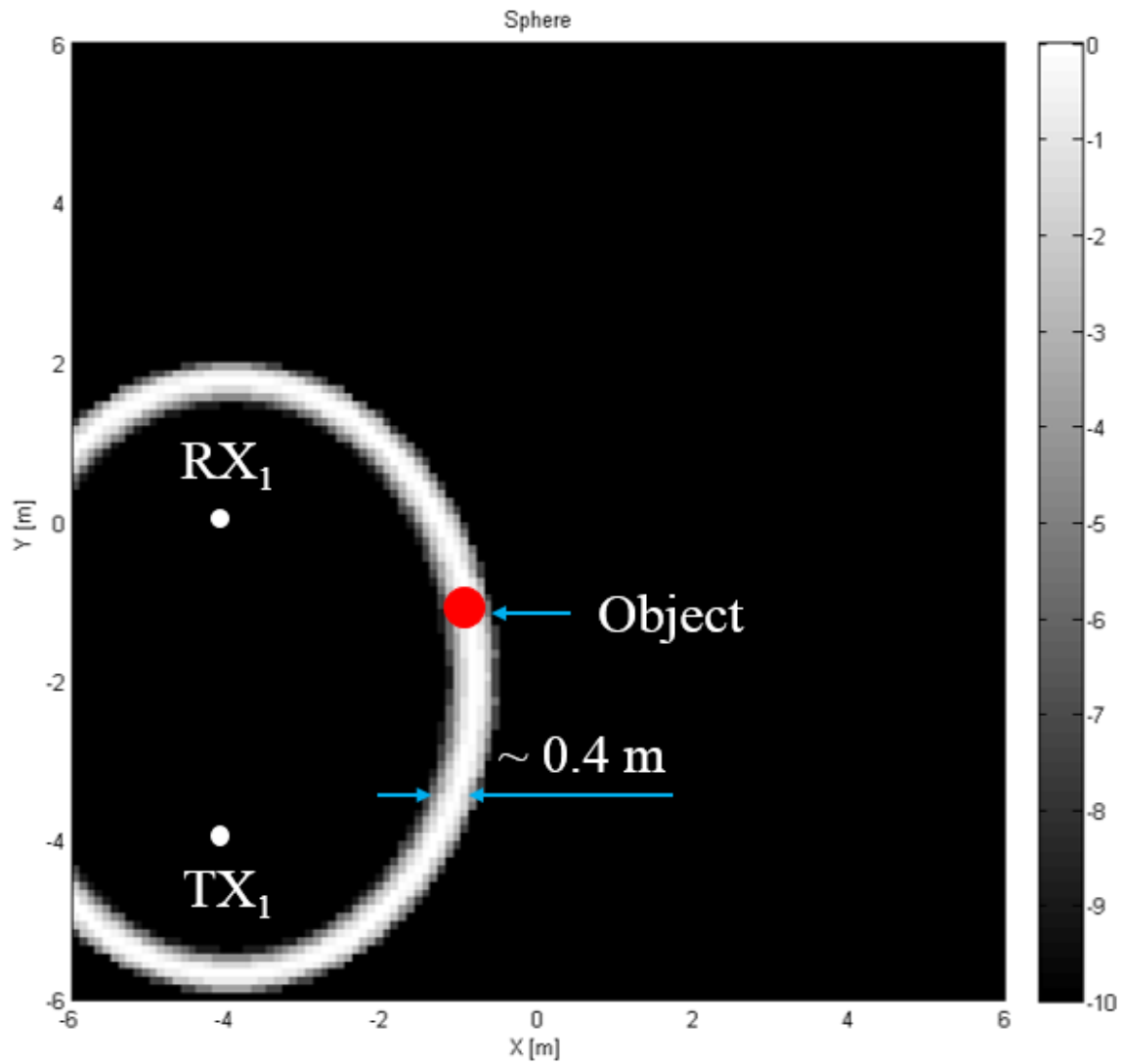
Figure 22: TX$_1$-RX$_1$ isorange contour

Expanding the result to contain two pairs of transmitters and receivers, the same result can be seen with the addition of one extra ellipse. The intersection point of these two contours is exactly where the object is. Figure 23 illustrates this case.
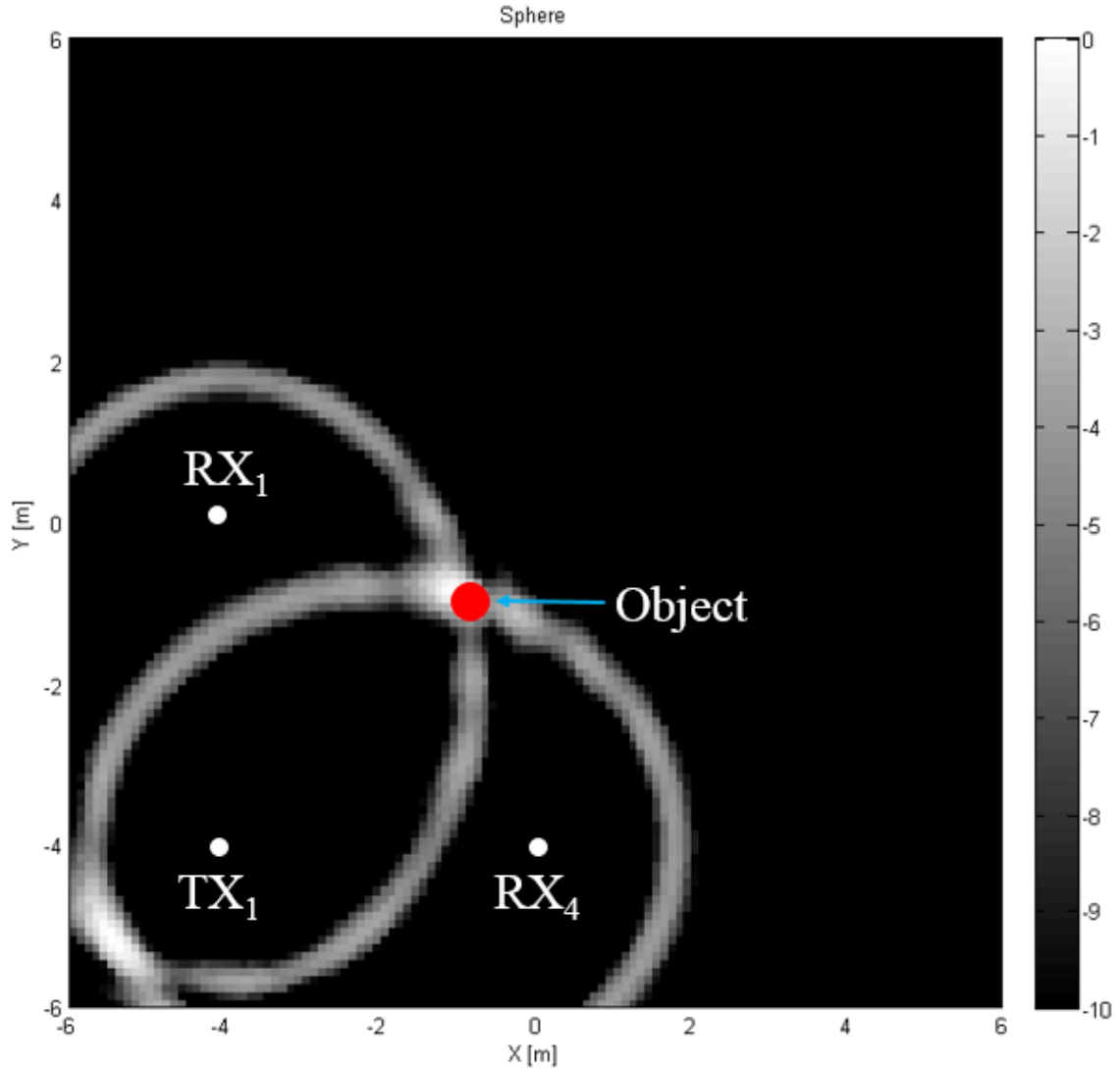
Figure 23: TX_1-RX_1 and TX1-RX_4 isorange contours. The intersection locates the object.

With three and four pairs of transmitters and receivers, similar results are achieved, as shown in Figure 24 and Figure 25. The ellipses still share one common point at the location of the object; however, there is a secondary strong peak near $(-5, -2)$, which is not the object location. This peak is regarded as a ghost object and may be ignored by inspecting the blind regions of each receiver. For example, in this case, this

ghost object is in the blind region of RX_1 with respect to TX_1, therefore, it can be safely disregarded as a real object. Another simple method to eliminate ghost objects is by ignoring the regions outside of the imaging grid. For example, the ghost object in Figure 24 can be easily identified and ignored because it's outside of the region of interest (superimposed yellow square.)
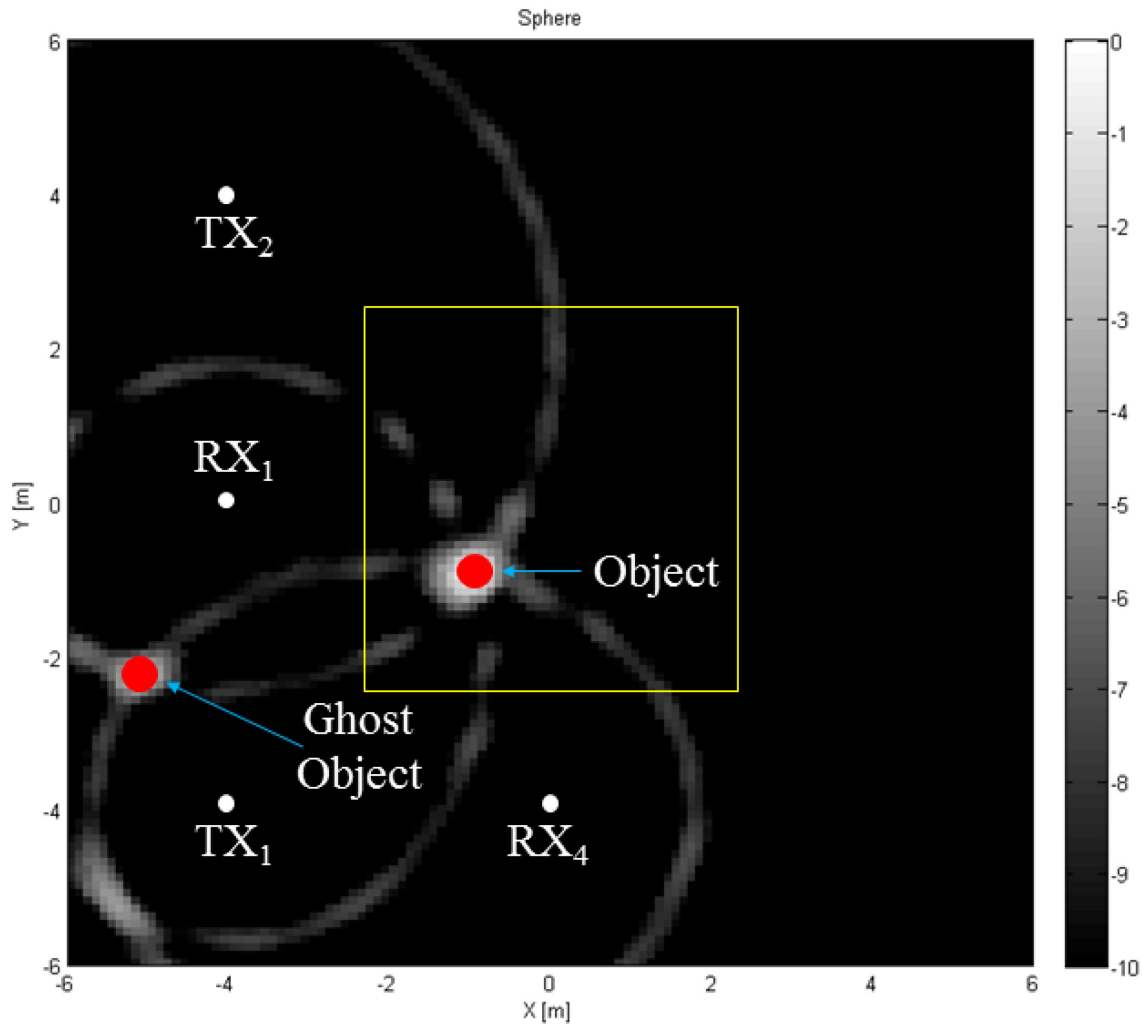

Figure 24: Isorange contours of TX_1-RX_1, TX_1-RX_4, and TX_2-RX_1 with a ghost object
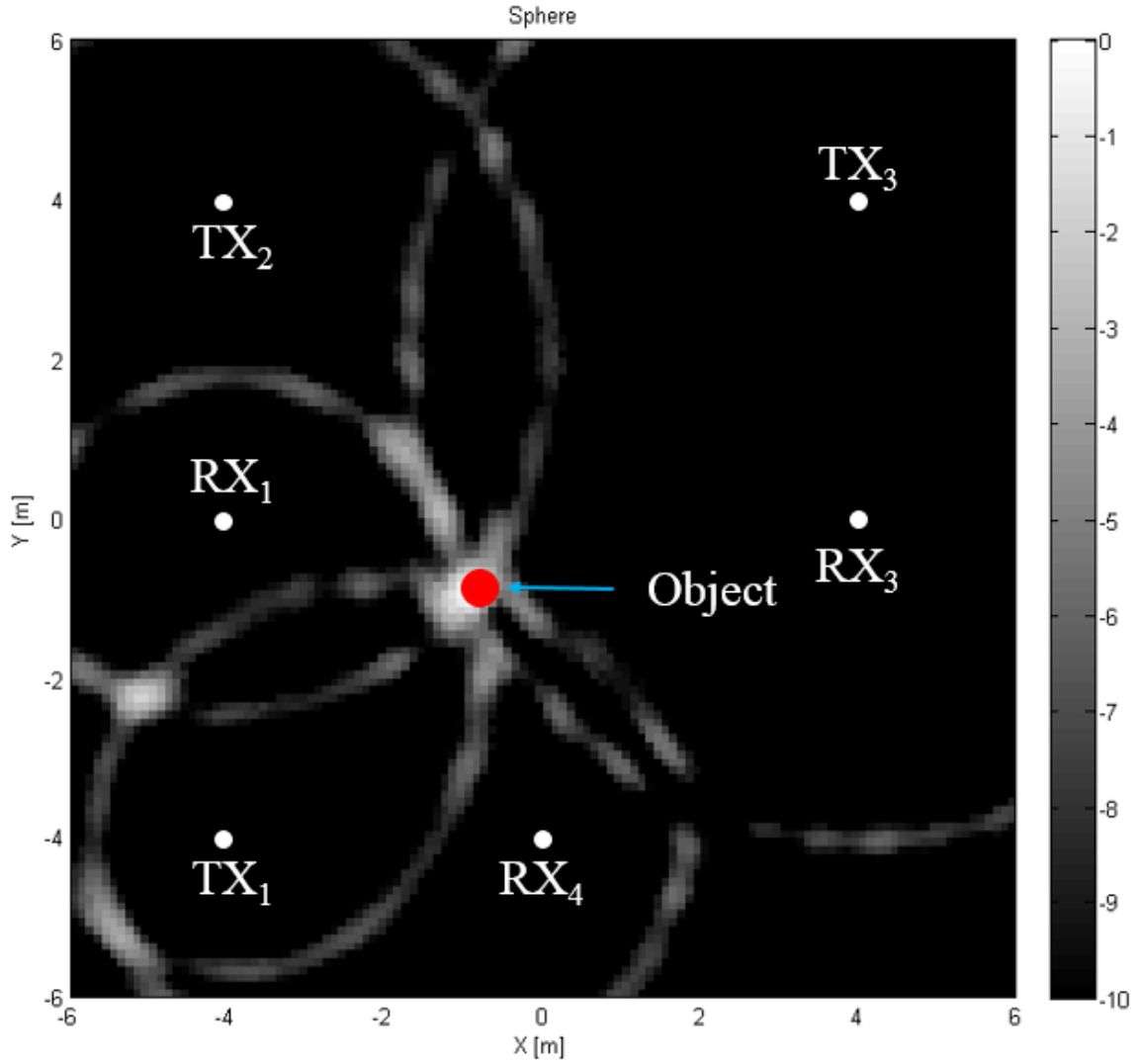
Figure 25: Isorange contours of TX_1-RX_1, TX_1-RX_4, TX_2-RX_1, and TX_3-RX_3

Finally, with every pair of transmitter and receiver data, a complete tomographic image of the scene of interest can be constructed, as shown in Figure 26. This image is generated by plotting vector $\mathbf{y} = \mathbf{L}^H \cdot \mathbf{s}$ in its original form. Because the hardware setup consists of four transmitters and four receivers, the total number of isorange contours is sixteen. They all intersect at $(-1, \ -1)$, where the object is expected to be.
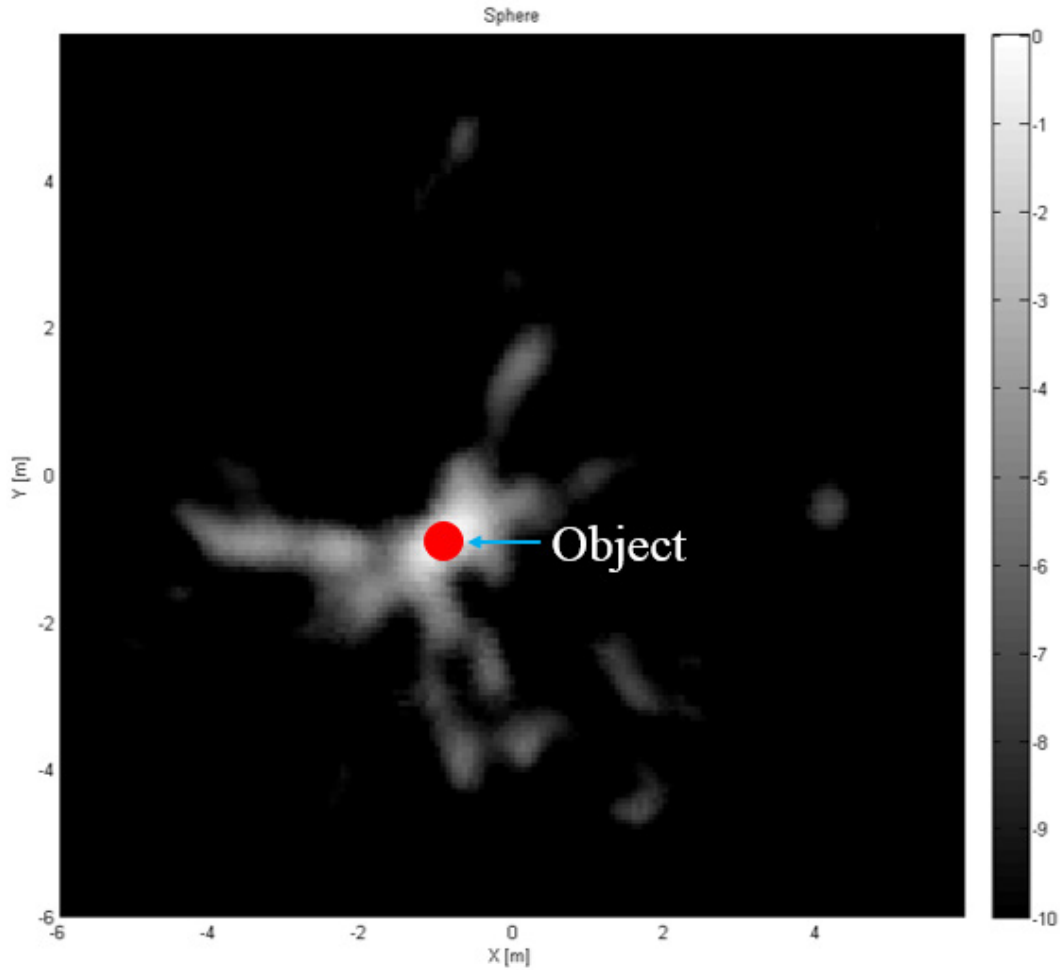
Figure 26: Complete tomographic image using information from all four transmitters and

four receivers, for a total of sixteen isorange contours

Examining Figure 22 through Figure 25, it is evident that the greater the number of transmitter and receiver pairs used in reconstruction, the more defined the object is in the formed image. This is because when the intensity of the intersection of all ellipses is coherently added, object's magnitude is much greater than that of the remaining points in the ellipses. In other words, the SNR increases proportionally with the number of data points.

The interference pattern in Figure 26, however, may create difficulties in determining the actual object location. To remedy this, another plotting method is employed. A new image is formed by plotting the absolute value of vector **y**, i.e., $\mathbf{y} = \left|\mathbf{L}^H\right| \cdot |\mathbf{s}|$, shown in Figure 27. This results in the loss of phase information, thus decreasing the SNR; nonetheless, it is still possible to determine the object location by searching for the absolute peak of the intensity. In this plot, the highest peak is determined by the strongest white spot in the middle region.
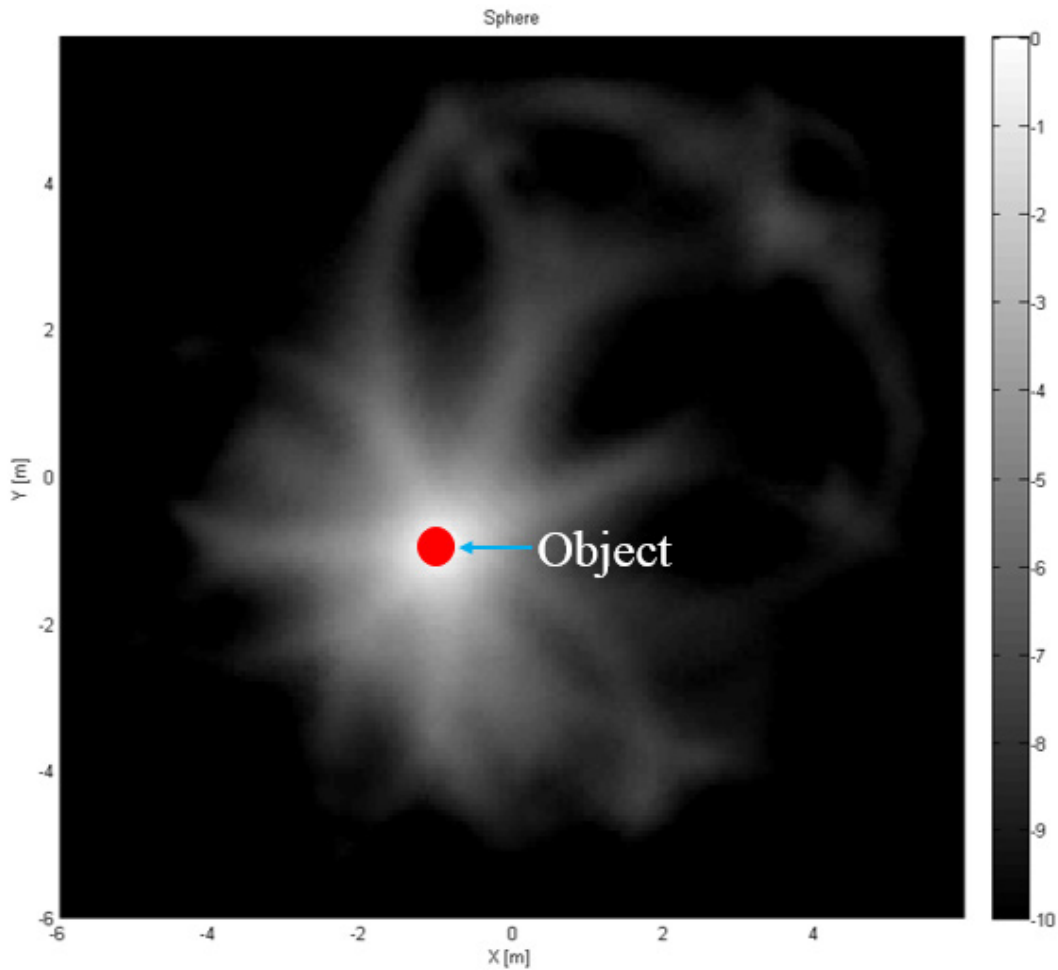
Figure 27: Image constructed by plotting the absolute value of vector **y**, where phase information is ignored

With data from all possible pairs of transmitter and receiver, there is noticeable interference around the object area, as evident in Figure 26 and Figure 27. To alleviate this effect and make object detection easier, some sets of data may be taken out. To determine which results to discard, plotting every set of data reveals the undesirables, as shown in Figure 28.
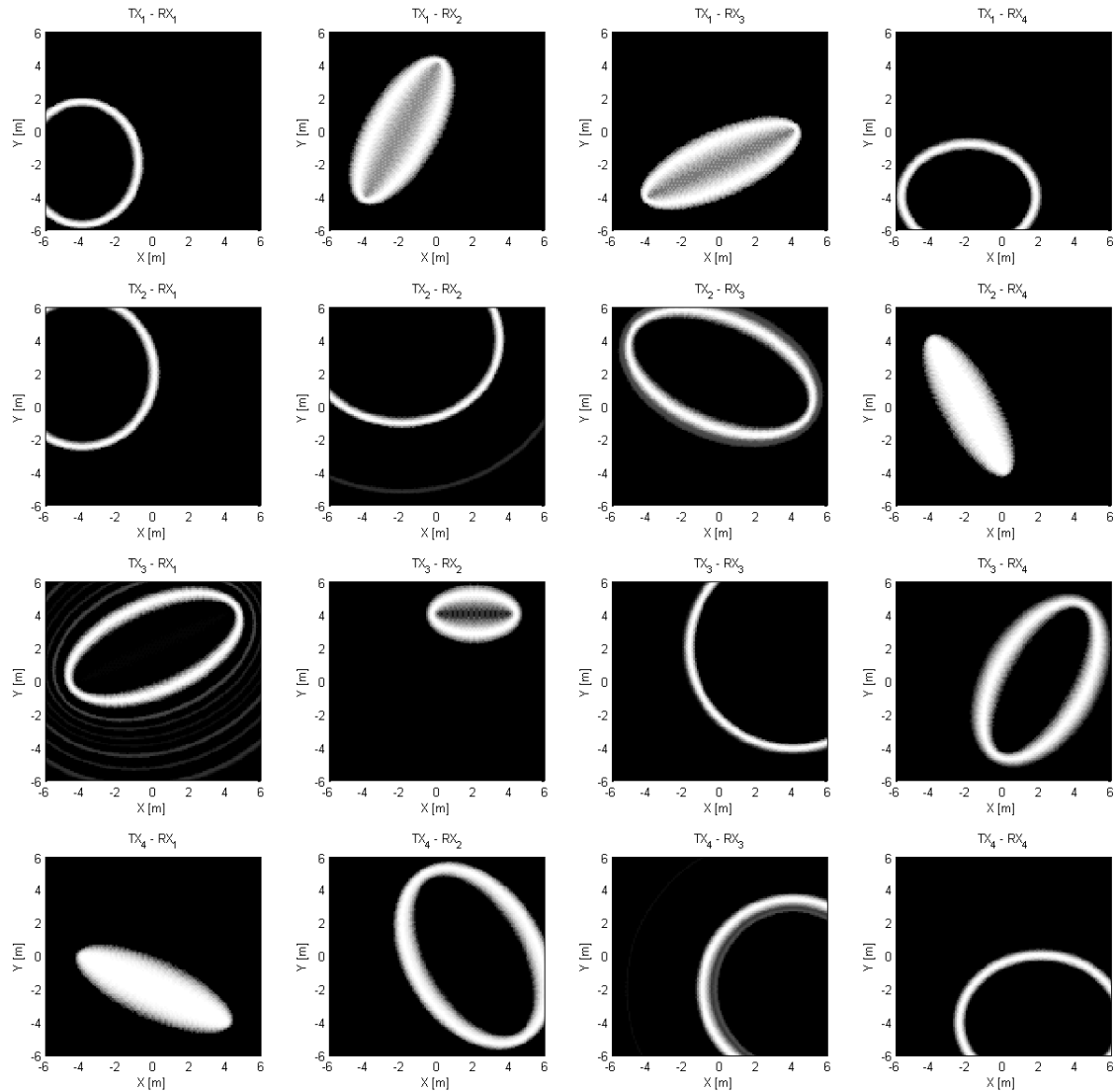
Figure 28: Plots of all sets of transmitter and receiver data

From these individual plots, it is easy to identify three possible types of problems. One of them is multiple returns, as evident from the plots of TX_2-RX_2, TX_3-RX_1, and TX_4-RX_3. A possible explanation of this problem is that the experiment was conducted indoors with strong clutter returns from metal objects inside the test facility. The second problem may be that when the transmitter, object, and receiver are nearly in a straight line, as shown in the plots of TX_1-RX_2, TX_1-RX_3, TX_2-RX_4, and TX_4 –RX_1, the resulting images are not as clear as other isorange contours. Recall from the bistatic range resolution in Section 2.3.3 and derivation of the receiver's blind region in Section 3.5.2, the receiver cannot distinguish between direct-path and echo signals if the transmitter, object, and receiver line up in that order. In this case, when the bistatic angle is almost 180°, the range resolution breaks down. The last problem appears when the clutter returns are stronger than those of the objects. This happens when background subtraction takes place. If the object echoes appear to be weaker than the background reference, as described early in this section, the object will be discarded as part of the background. The resulting images are thus incorrect, as shown in the plot of TX_3-RX_2.

After identifying the troubled data sets and discarding them, new images are reconstructed using the same method as before. These new images have less interference, and object detection is easier compared to Figure 26 and Figure 27. Figure 29 illustrates this result.
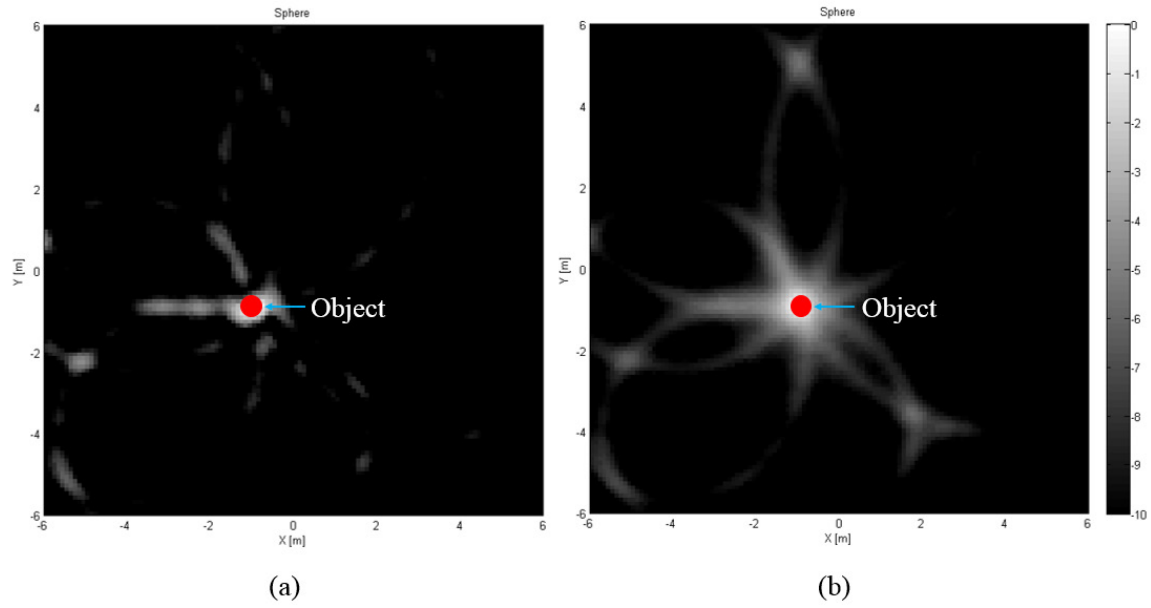
Figure 29: Reconstructed images in which undesirable data sets are manually taken out.

Vector. (a) Plot of complex data $\left(\mathbf{y} = \mathbf{L}^{H} \cdot \mathbf{s}\right)$. (b) Plot of absolute values $\left(\mathbf{y} = \left|\mathbf{L}^{H}\right| \cdot |\mathbf{s}|\right)$

V. Discussion and Conclusion

5.1   Chapter Overview

This chapter summarizes this thesis by recapping the accomplishments as well as shortcomings of the passive RF tomography research. First, an overview of the theory along with the signal processing procedure is given. The proof of concept experiment setup and results also are reviewed. Finally, this thesis concludes with recommendations for future work.

5.2   Summary of Theory

This research has expanded upon the previous passive RF tomography work by broadening the theory with additional concepts, as well as providing a proof of concept by means of hardware experimentation. The concept of RF tomography has been explored in recent literature with many applications in ground penetrating radars and tunnel detection. Passive RF tomography eliminates the active transmitters and relies only on the signals of opportunity presumably already present in the environment. This mode of operation allows the hardware implementation to be more cost-effective and provides the added benefit of frequency compliance due to the lack of transmitters; however, the signal processing requires advanced methodology and solutions. There are certain conditions the signals of opportunity have to meet for the algorithm to work. The most important assumptions are that the incoming waveforms have to be similar to radar signals, or LFM chirps. They also have to be separated in time and frequency. The transmitters are assumed to be infinitely far from the receivers and scene of interest for their transmitted wavefronts to be planar.

The methodology developed in this research relies on the knowledge of the receivers' locations and estimated directions of the signals of opportunity for image reconstruction. The procedure progresses as follows:

1. Identification of Signals of Opportunity - The system scans the surrounding environment of the scene of observation. Captured data are analyzed for radar signals suitable for detection and imaging purposes.

2. Differentiation between Incident and Scattered Signals - Recorded data are divided into incident and scattered signals. Incident, or direct path, signals come directly from the transmitters. Scattered signals, or echoes, are reflections from objects illuminated by the same direct path waveforms.

3. Estimation of the Time Differences of Arrivals - Once the signals of opportunity are identified and separated, the TDOA for each transmitter and receiver pair is calculated for the next step.

4. Source Localization - TDOA information is used to estimate the direction of incoming wavefronts. Because transmitters' exact locations are unknown, they have to be approximated through the bearing angles of the sources of opportunity.

5. RF Tomography in Time Domain - A modified version of RF tomography is applied to the matched filtered scattered returns, using the estimated direction of each transmitter instead of its exact location.

These steps are applied to captured data from an experiment conducted with a hardware implementation. This test system consists of four transmitters and four receivers. Each independent transmitter radiates a different waveform that conforms to

72

the assumptions laid out in Section 1.2. These waveforms illuminate a scene of interest where possible objects are present. If there is an object, the reflectivity measured in the backscattered signal is greater than zero; otherwise, the magnitude of the echo is zero. With four pairs of transmitters and receivers, there are sixteen data sets to process. Each set of received data consists of two parts: direct-path and echo. Finally, by applying the methodology of passive RF tomography, an image is reconstructed based on all different perspective views of each receiver. Obtained results are analyzed to confirm the theory and methodology, as well as to reveal the successes and shortcomings of the experiment.

5.3   Experiment Accomplishments

Results obtained from the hardware implementation show that the methodology developed in this research performs properly and accurately under the assumptions outlined in Chapter 1. With one object in the scene of imaging, the algorithm produces expected results. Individual plots of processed data from each pair of transmitter and receiver demonstrate the isorange contours in the shape of an ellipse whose foci coincide with the transmitter's and receiver's locations. When all sixteen data sets are superpositioned on one plot, the single object located at $(-1, -1)$ is identified by its highest peak; furthermore, the derivation of the receiver's blind region is also proved to be correct in cases when the transmitter, object, and receiver are in a near straight line. This geometry approaches the point at which the range resolution is no longer valid. This rendered object detection difficult and inaccurate. After identifying and discarding these troubling data sets, the final reconstructed image is cleaner and has less ambiguity and interference around the object location. Finally, the results also suggest that the hardware

system constructed for this experiment is proven for this type of operation; therefore, both goals of this research are achieved.

5.4   Future Work Recommendations

The results demonstrated in Chapter 4 have several weaknesses that can be addressed if future funding continues. First, an experiment carried out in an open environment can improve results due to reduced clutter and interference. It was not possible to experiment in an open environment due to the lack of manpower, time, and funding in planning and execution; furthermore, the hardware went through multiple revisions in the prototyping phase because such a low-cost and mobile system had never been built before at AFRL.

Another recommendation for future work is a multiple-object experiment setup. Because the methodology was developed for more than one objects, this test should be possible with few to no changes in the algorithm as well as the hardware; however, it may be better to attempt this experiment outdoors or in an anechoic chamber to avoid false positives coming from indoor clutter.

Finally, the theory may be expanded to include detection of moving objects. Doppler processing is a useful addition to the methodology to make the theory more complete and applicable to realistic scenarios. Additionally, the experiment could be modified to accommodate a three-dimensional imaging area in which objects can have movements in the z-direction. This extension could increase the number of possible applications for both military and civilian purposes.

Bibliography

[1] L. Lo Monte, D. Erricolo, F. Soldovieri and M. Wicks, "Underground imaging of irregular terrains using RF Tomography," *3rd IEEE International Workshop on Computational Advances in Multi-Sensor Adaptive Processing (CAMSAP),* pp. 13-16, 2009.

[2] L. Lo Monte, M. Wicks, F. Soldovieri and D. Erricolo, "Toward a complete forward model for underground imaging Using RF tomography," *6th International Workshop on Advanced Ground Penetrating Radar (IWAGPR),* pp. 22-24, 2011.

[3] L. Lo Monte, D. Erricolo, V. Picco, F. Soldovieri and M. Wicks, "Distributed RF tomography for tunnel detection: Suitable inversion schemes," *Proceedings of the IEEE 2009 National Aerospace & Electronics Conference (NAECON),* pp. 21-23, 2009.

[4] X. Chen, A. Edelstein, Y. Li, M. Coates, M. Rabbat and A. Men, "Sequential Monte Carlo for simultaneous passive device-free tracking and sensor localization using received signal strength measurements," *10th International Conference on Information Processing in Sensor Networks (IPSN),* pp. 342,353, 12-14, 2011.

[5] R. Saini, M. Cherniakov and V. Lenive, "Direct path interference suppression in bistatic system: DTV based radar," *Proceedings of the International Radar Conference,* pp. 3-5, 2003.

[6] H. Meikle, Modern Radar Systems, Boston: Artech House, 2001.

[7] R. G. Wiley, ELINT, The Interception and Analysis of Radar Signals, Norwood, MA: Artech House, 2009.

[8] L. Lo Monte, M. Wicks and W. Barott, "RF Tomography using radars of opportunity: Theory and experimental validation," in *IEEE Radar Conference (RADAR)*, 2013.

[9] D. J. Munson, J. O'Brien and W. Jenkins, "A tomographic formulation of spotlight-mode synthetic aperture radar," *Proceedings of the IEEE,* vol. 71, no. 8, pp. 917-925, 1983.

[10] G. T. Herman, Fundamentals of computerized tomography: image reconstruction from projections, 2nd ed., New York: Springer, 2009.

[11] E. Ertin, C. D. Austin, S. Sharma, R. L. Moses and L. C. Potter, "GOTCHA experience report: Three-dimensional SAR imaging with," *Algorithms for Synthetic Aperture Radar Imagery XIV,* vol. 6568, no. SPIE, 2007.

[12] M. Cheney and B. Borden, Fundamentals of Radar Imaging, SIAM, 2009.

[13] J. E. Greivenkamp, "Field Guide to Geometrical Optics," *SPIE Field Guids,* vol. 1, 2004.

[14] P. Z. Peebles, Radar Principles, New York: Wiley-Interscience, 1998.

[15] R. Nitzberg, Radar signal processing and adaptive systems, Boston: Artech House, 1999.

[16] G. Turin, "An introduction to matched filters," *IRE Transactions on Information Theory,* vol. 6, no. 3, pp. 311-329, 1960.

[17] M. A. Richards, Fundamentals of Radar Signal Processing, New York: McGraw Hill Professional, 2005.

[18] N. J. Willis, Bistatic Radar, Edison, NJ: SciTech Publishing, 2005.

[19] D. L. Mensa, High resolution radar cross-section imaging, Boston, MA: Artech House, 1991.

[20] L. Lo Monte, D. Erricolo, F. Soldovieri and M. Wicks, "RF Tomography for Below-Ground Imaging of Extended Areas and Close-in Sensing," *IEEE Geoscience and Remote Sensing Letters,* vol. 2010, pp. 496-500, 2010.

[21] L. Lo Monte and J. Parker, "Sparse reconstruction methods in RF Tomography for underground imaging," *International Waveform Diversity and Design Conference (WDD),* pp. 28-32, 2010.

[22] L. Lo Monte, D. Erricolo, F. Soldovieri and M. C. Wicks, "Radio Frequency Tomography for Tunnel Detection," *IEEE Transactions on Geoscience and Remote Sensing,* vol. 48, no. 3, pp. 1128-1137, 2010.

[23] M. Wicks, "RF Tomography with Application to Ground Penetrating Radar," *Conference on Signals, Systems and Computers,* pp. 2017-2022, 2007.

[24] K. Kulpa, M. Malanowski, J. Misiurewicz and P. Samczynski, "Passive radar for strategic object protection," *2011 IEEE International Conference on Microwaves, Communications, Antennas and Electronics Systems (COMCAS),* pp. 7-9, 2011.

[25] M. Malanowski, K. Kulpa, P. Samczynski, J. Misiurewicz, J. Kulpa, P. Roszkowski, P. Dzwonkowski, D. Gromek, L. Maslikowski, M. Misiurewicz and L. Podkalicki, "Experimental results of the PaRaDe passive radar field trials," *13th International Radar Symposium (IRS),* pp. 23-25, 2012.

[26] M. Malanowski, K. Kulpa, P. Samczynski, J. Misiurewicz and J. Kulpa, "Long range FM-based passive radar," *IET International Conference on Radar Systems (Radar 2012),* pp. 22-25, 2012.

[27] P. Samczynski and K. Kulpa, "Passive SAR imaging using a satellite pulsed radar as an illuminator of opportunity," *13th International Radar Symposium (IRS),* pp. 23-25, 2012.

[28] G. Strang, Linear Algebra and Its Applications, Belmont: Cengage Learning, 2006.

[29] J. T. Parker, M. Ferrara, J. Bracken and B. Himed, "Preliminary experimental results for RF tomography using distributed sensing," *International Conference on Electromagnetics in Advanced Applications (ICEAA),* pp. 549-552, 2010.

Vita

The author Thang M. Tran earned Associate Degrees at Carl Albert State College in Poteau, Oklahoma in 2007. He then moved to Ohio and was graduated summa cum laude from Wright State University in 2010 with a Bachelor of Science in Electrical Engineering. After that, he worked as an electronics engineer for two years before pursuing his Master of Science in Electrical Engineering at the Air Force Institute of Technology.

REPORT DOCUMENTATION PAGE				*Form Approved* *OMB No. 074-0188*

The public reporting burden for this collection of information is estimated to average 1 hour per response, including the time for reviewing instructions, searching existing data sources, gathering and maintaining the data needed, and completing and reviewing the collection of information. Send comments regarding this burden estimate or any other aspect of the collection of information, including suggestions for reducing this burden to Department of Defense, Washington Headquarters Services, Directorate for Information Operations and Reports (0704-0188), 1215 Jefferson Davis Highway, Suite 1204, Arlington, VA 22202-4302. Respondents should be aware that notwithstanding any other provision of law, no person shall be subject to an penalty for failing to comply with a collection of information if it does not display a currently valid OMB control number.
PLEASE DO NOT RETURN YOUR FORM TO THE ABOVE ADDRESS.

1. REPORT DATE *(DD-MM-YYYY)* 27-03-2014	2. REPORT TYPE Master's Thesis		3. DATES COVERED *(From – To)* Apr 2012 - Mar 2014	

4. TITLE AND SUBTITLE Passive RF Tomography: Signal Processing and Experimental Validation	5a. CONTRACT NUMBER
	5b. GRANT NUMBER
	5c. PROGRAM ELEMENT NUMBER
6. AUTHOR Tran, Thang M., Civilian Student, USAF	5d. PROJECT NUMBER
	5e. TASK NUMBER
	5f. WORK UNIT NUMBER

7. PERFORMING ORGANIZATION NAMES(S) AND ADDRESS(S) Air Force Institute of Technology Graduate School of Engineering and Management (AFIT/EN) 2950 Hobson Way WPAFB OH 45433-7765	8. PERFORMING ORGANIZATION REPORT NUMBER AFIT-ENG-14-M-91

9. SPONSORING/MONITORING AGENCY NAME(S) AND ADDRESS(ES) Air Force Research Laboratory, Sensors Directorate, RF Technology Branch Attn: Gary J. Scalzi RF Technology Branch, Sensors Directorate (AFRL/RYMD) 2241 Avionics Circle, Bldg 620, WPAFB, OH 45433 937-528-8131 gary. scalzi@wpafb.af.mil	10. SPONSOR/MONITOR'S ACRONYM(S) AFRL/RYMD
	11. SPONSOR/MONITOR'S REPORT NUMBER(S)

12. DISTRIBUTION/AVAILABILITY STATEMENT DISTRIBUTION STATEMENT A: APPROVED FOR PUBLIC RELEASE; DISTRIBUTION UNLIMITED.

13. SUPPLEMENTARY NOTES This material is declared a work of the U.S. Government and is not subject to copyright protection in the United States.

14. ABSTRACT Radio frequency (RF) tomography is an imaging technique based upon a set of distributed transmitters and receivers surrounding the area under observation. This method requires prior knowledge of the transmitters' and receivers' locations. In some circumstances the transmitters may be uncooperative, while in other cases extrinsic emitters may be used as source of opportunity. In these scenarios, RF tomography should operate in a passive modality. A previous work postulated the principles and feasibility of passive RF tomography. This research further develops the underlying theory through concise and ad-hoc signal processing. Experimental verification and validation corroborate the effectiveness of passive RF tomography for object detection and imaging.

15. SUBJECT TERMS Passive Radar, RF Tomography, Radar Imaging, Detection

16. SECURITY CLASSIFICATION OF:			17. LIMITATION OF ABSTRACT	18. NUMBER OF PAGES	19a. NAME OF RESPONSIBLE PERSON Andrew J. Terzuoli (AFIT/ENG)
REPORT U	ABSTRACT U	c. THIS PAGE U	UU	94	19b. TELEPHONE NUMBER *(Include area code)* (937) 255-3636 x4717 andrew.terzuoli@afit.edu

Standard Form 298 (Rev: 8-98)
Prescribed by ANSI Std. Z39-18